UNIVERSIDADE DE LISBOA
FACULDADE DE CIÊNCIAS
DEPARTAMENTO DE QUÍMICA E BIOQUÍMICA

Competition Between Halogen and Hydrogen Bonds and Stability of Celecoxib-Tramadol·HCl Cocrystal and Coamorphous Nanoparticles

Daniel Filipe Valente Matias

Mestrado em Química
Especialização em Química

Dissertação orientada por:
Professor Manuel Minas da Piedade
Professora Maria da Soledade Santos

2023

Aos meus pais

Agradecimentos

A presente tese não resulta de um esforço individual, mas sim da cristalização de uma colaboração, tanto direta como indireta, de diversas pessoas e instituições, às quais deixo, nesta pequena secção, o meu reconhecimento e agradecimento.

Em primeiro, ao Professor Manuel Minas da Piedade que criou a semente para este trabalho aceitando-me no seu laboratório e fornecendo valorosas oportunidades, às quais sinto-me grato.

À Professora Maria da Soledade Santos pelas sugestões, conversas e revisões que me permitiram elevar o nível deste trabalho.

Ao Dr. Carlos Bernardes pela disponibilidade, conhecimento e todo o apoio que me forneceu ao longo destes anos.

Ao Professor Hermínio Diogo pela disponibilização e ajuda com os aparelhos de TSDC e HSM e ainda por toda a prontidão na ajuda com a aprendizagem das técnicas e com as análises de resultados. À Doutora Franziska Emmerling pela oportunidade de realizar experiências nos laboratórios do *Helmholtz Centre Berlin for Materials and Energy* e na linha de sincrotrão BESSY II no *Helmholtz-Zentrum Berlin*. À Professora Fátima Piedade e à Inês Feliciano pelas determinações das estruturas cristalinas. Ao Aaron O'Sullivan e ao Professor Luís Padrela do *SSPC Research Centre* na Irlanda pelas amostras de nanopartículas e pelos resultados de solubilidade. A todos os colegas e amigos pelas conversas e discussões que me permitiram aprimorar a qualidade do meu trabalho.

Aos meus amigos com os quais tive de abdicar de algum tempo para dedicar a este trabalho.

À Beatriz Ferreira por todo o apoio, paciência e amor.

Ao meu irmão que sempre me motivou e me guiou ao longo destes anos.

Por último, à minha mãe e ao meu pai que sempre fizeram tudo para que não me faltasse nada.

What I say of science here, I say without condition, that science is the latest and the greatest superstition.

Louis Hardin

Resumo

Os co-cristais são uma das mais promissoras tecnologias desenvolvidas pela engenharia de cristais para melhorar as propriedades de materiais sólidos. Devido ao enorme número de combinações possíveis entre diferentes moléculas, os co-cristais permitem a manipulação das propriedades de materiais relevantes em várias indústrias, como a dos materiais energéticos, dos agroquímicos e, atualmente, sobretudo da indústria farmacêutica.

Visto que a formação de co-cristais está dependente dos tipos e quantidade de interações intermoleculares possíveis de serem estabelecidas entre as moléculas, o estudo deste tipo de interações e da forma como competem entre si é fundamental para o desenvolvimento de estratégias de síntese de co-cristais eficazes. Historicamente, as ligações intermoleculares mais estudadas são as ligações de hidrogénio, as interações de van der Waals e as interações de Coulomb. No entanto, durante o século XIX um novo tipo de interações com uma força semelhante às ligações de hidrogénio foi descoberta – as ligações de halogénio. Devido aos avanços computacionais, no final do século XX, foi possível determinar a origem deste tipo de interações: a formação de uma ligação covalente com um átomo de halogénio retira densidade eletrónica da orbital antiligante deste, originando uma zona com menor densidade eletrónica oposta à ligação covalente. Assim, as ligações de halogénio são ligações direcionais e com carácter tanto electroestático como de doação de carga. As suas propriedades são, no entanto, muito semelhantes às das ligações de hidrogénio o que pode tornar difícil a previsão de quais vão ser formadas preferencialmente quando ambas são possíveis.

Neste trabalho realizou-se um estudo da competição/cooperação entre ligações de halogénio e hidrogénio na formação de co-cristais. Para efeito de obter co-cristais, utilizou-se a técnica de mecanoquímica com dois equivalentes de moléculas doadoras de ligações de halogénio e ligações de hidrogénio (halogenofenóis) para um equivalente de moléculas que aceitam ambas as ligações (pirazina, hexametilenotetramina e 1,4-diazobiciclo[2.2.2]octano). Foram produzidos 25 co-cristais novos (3 com a pirazina, 11 com o 1,4-diazobiciclo[2.2.2]octano e 11 com a hexametilenotetramina). As sínteses com pirazina produziram, na maioria dos casos, líquidos. Para 6 destes 25 co-cristais, foi possível determinar a estrutura cristalina por difração de raios-X de cristal único (3-clorofenol, 3-bromofenol e 4-iodofenol com o 1,4-diazobiciclo[2.2.2]octano e 4-clorofenol, 4-bromofenol e 4-iodofenol com a hexametilenotetramina). As estruturas cristalinas obtidas revelaram que nestes co-cristais, as ligações de hidrogénio são preferenciais, visto que todos os grupos hidroxilo estavam presentes numa ligação de hidrogénio com o aceitador. A estrutura do co-cristal de 4-iodofenol com o 1,4-diazobiciclo[2.2.2]octano evidenciou um arranjo molecular onde 4 átomos de halogénio formam uma série de 3 ligações halogénio-halogénio. O co-cristal do 4-iodofenol com a hexametilenotetramina mostrou a formação de uma ligação de halogénio paralelamente a duas ligações de hidrogénio, revelando a cooperação entre os dois tipos de interação. Um estudo preliminar da cinética das reações de formação dos co-cristais de 4-iodofenol e 4-bromofenol com 1,4-diazobiciclo[2.2.2]octano através de mecanoquímica, foi realizado usando difração de raios-X com radiação de sincrotrão. As reações foram muito rápidas (<1 min) o que impediu determinação de constantes de velocidade.

Adicionalmente, foi realizado um estudo computacional para determinar as energias de interação de diferentes dímeros de moléculas capazes de formar ou ligações de halogénio ou ligações de hidrogénio, correspondentes a combinações utilizadas na síntese dos co-cristais. Os cálculos

revelaram que: (*i*) as moléculas com flúor não formam ligações de halogénio. (*ii*) As ligações de hidrogénio são as mais fortes, seguidas pelas ligações de halogénio com as bases de azoto, seguidas das ligações de halogénio do tipo halogénio-halogénio. (*iii*) A alteração do átomo de halogénio tem um impacto na força de ligação de todos os tipos de interação. Este impacto é maior para as ligações de halogénio com as bases azotadas, seguidas pelas ligações de halogénio do tipo halogénio-halogénio e por fim as ligações de hidrogénio. (*iv*) A posição do grupo hidroxilo relativa ao átomo de halogénio tem, também, uma influência na força das interações sendo que as moléculas com os substituintes mais afastados, substituição *para*, resultou em menores forças de ligação, seguida da substituição *meta* e por fim a substituição *orto*.

A formação de co-cristais tem sido alvo de muita atenção. No entanto, os aspetos termodinâmicos relativos à formação deste tipo de materiais não foram ainda muito explorados. O segundo capítulo deste trabalho focou-se na análise térmica e na estabilidade termodinâmica de um co-cristal recentemente descoberto envolvendo a combinação dos medicamentos celecoxibe (usado como anti-inflamatório) e o hidrocloreto de tramadol (usado para o tratamento de dor moderada a severa). Este co-cristal está já a ser comercializado sob a designação Seglentis®. Para além da forma cristalina, foram analisadas amostras de nanopartículas cristalinas e amorfas (com tamanhos de partícula diferentes) de uma mistura de celecoxibe com hidrocloreto de tramadol produzidas através de *CO_2-assisted nano-spray drying*. O estudo permitiu avaliar o impacto do tamanho de partícula e da organização molecular na estabilidade dos materiais. Os resultados de termogravimetria demonstraram que a decomposição térmica destes materiais bicomponentes tem um comportamento intermédio ao dos dois precursores. Os resultados de calorimetria diferencial de varrimento (DSC) das amostras cristalinas corroboram os dados da literatura, os das amostras amorfas evidenciaram uma cristalização fria, a cerca de 390 K, confirmada por microscopia *hot-stage*, seguida da fusão do co-cristal.

A estabilidade destes materiais foi estudada com base na energia de Gibbs da reação de decomposição nos precursores. O termo entálpico foi determinado com recurso à calorimetria de solução e a resultados de DSC, permitindo a comparação dos dois métodos, e a energia de Gibbs foi determinada através de medidas de solubilidade. O fator entrópico pôde posteriormente ser deduzido através destas duas grandezas. Os resultados obtidos por calorimetria de solução revelaram que, em termos entálpicos: (*i*) apenas o co-cristal produzido por cristalização a partir da solução é estável; (*ii*) as nanopartículas cristalinas são ligeiramente instáveis e as nanopartículas amorfas são muito instáveis; (*iii*). a diminuição do tamanho de partícula aumenta a instabilidade da amostra. Os dados obtidos por DSC apenas concordaram com a informação recolhida por calorimetria de solução em termos das amostras cristalinas serem mais estáveis que as amostras amorfas, não tendo sido detetada a diferença de estabilidade entre as duas amostras cristalinas ou e uma relação clara entre o tamanho de partícula e a estabilidade. É de salientar que os resultados obtidos por este método apresentaram valores absolutos sobrestimados relativamente aos obtidos por calorimetria de solução. Sendo que ambos os métodos são comumente utilizados para a medição desta grandeza, mais estudos têm de ser realizados de modo a compará-los e determinar a sua validade. A determinação da energia de Gibbs foi realizada apenas para as amostras cristalinas, visto que, as amostras amorfas aparentam degradar-se aquando do contacto com o solvente, não sendo os valores de solubilidade representativos das mesmas. A análise dos valores obtidos para a estabilidade termodinâmica em termos de energia de Gibbs, revelam que: (*i*) ambas as amostras cristalinas são estáveis face à decomposição nos seus precursores, $\Delta_r G°_m > 0$; (*ii*) A estabilidade da amostra de co-cristal produzida por cristalização de solução aparenta ser de natureza entálpica, $\Delta_r H°_m > |T\Delta_r S°_m|$, enquanto a estabilidade da amostra de co-cristal produzida por *spray-drying* aparenta

ser de natureza entrópica, $\Delta_r H°_m < |T\Delta_r S°_m|$. Estes resultados suportam a interpretação de que uma diminuição do tamanho de partícula aumenta o número de moléculas à superfície, reduzindo simultaneamente o número de moléculas no interior do cristal, diminuindo a energia interna e aumentando a entropia.

Palavras-chave: Co-cristais, Ligações de Halogénio, Ligações de Hidrogénio, Energética.

Abstract

Cocrystals have, over the years, gained considerable interest due to their potential to improve material properties without changing the molecular structure. In this work, two studies were performed, the first involving a fundamental study on how hydrogen and halogen bonds compete/cooperate, in the formation of a cocrystal, the second concerning the thermodynamic stability of a Tramadol·HCL:Celecoxib cocrystal and its comparison with recently described coamorphous nanoparticles and cocrystalline nanoparticles produced through CO_2 assisted nano spray drying.

The study of halogen and hydrogen bonds competition/cooperation involved a cocrystal screening with donor (halogenophenols) acceptor (pyrazine, hexamethylenetetramine and 1,4-diazabicyclo[2.2.2]octane) molecules that could form both types of bonds. 25 new cocrystals were synthesized and 6 had the structure determined. Only one of the structures (4-iodophenol with hexamethylenetetramine) resulted in the formation of a halogen bond, despite the concomitant presence of two hydrogen bonds. All other structures only presented hydrogen bonds between the donor and acceptor molecules. Computed interaction energies between dimers of halogenophenols with 1,4-diazabicyclo[2.2.2]octane revealed that: (*i*) hydrogen bonds are the strongest among the studied interactions; (*ii*) the ring substituent pattern impacts the bond strength with closer substituents resulting in stronger bonds; (*iii*) changing the halogen atom affords an increase of the bond strength as we go down on the periodic table halogen group, an effect enhanced for halogen-halogen bonds.

Solution calorimetry and solubility measurements of the Tramadol·HCL:Celecoxib crystalline and amorphous samples revealed that: (*i*) both crystalline samples are stable against decomposition into their precursors, $\Delta_r G°_m>0$; (*ii*) the stability of the cocrystal produced through solution crystallization is of enthalpic nature, $\Delta_r H°_m>|T\Delta_r S°_m|$, while the stability of the cocrystalline sample produced through spray drying is of entropic nature, $\Delta_r H°_m<|T\Delta_r S°_m|$; (*iii*) on enthalpic grounds, smaller particle sizes seem to correlate with higher instability. (*iv*) amorphous samples presented lower stability.

Keywords: Cocrystals, Halogen Bonds, Hydrogen Bonds, Energetics.

Table of Contents

Table List

Figure List

List of Abbreviations

HB	Hydrogen bond
X	Halogen
B	Electron donor group
XB	Halogen bond
DAB	1,4-Diazabicyclo[2.2.2]octane
PYR	Pyrazine
HMT	Hexamethylenetetramine
DCM	Dichloromethane
2FP	2-Fluorophenol
3FP	3-Fluorophenol
4FP	4-Fluorophenol
2CP	2-Chlorophenol
3CP	3-Chlorophenol
4CP	4-Chlorophenol
2BP	2-Bromophenol
3BP	3-Bromophenol
4BP	4-Bromophenol
2IP	2-Iodophenol
3IP	3-Iodophenol
4IP	4-Iodophenol
4IA	4-Iodoaniline
1F4IB	1-Fluoro-4-iodobenzene
1I4IB	1,4-Diiodobenzene
1B4IB	1-Bromo-4-iodobenzene
1B4BB	1,4-Dibromobenzene
1B4CB	1-Bromo-4-chlorobenzene
1C4IB	1-Chloro-4-iodobenzene
PXRD	Powder X-Ray Diffraction
SCXRD	Single-Crystal X-Ray Diffraction
λ	Wavelenght
E_{int}	Interaction Energy
T	Temperature
a	Unit cell vector a lenght
b	Unit cell vector b lenght
c	Unit cell vector c lenght
α	Angle between vector *c* and *b* in the unit cell
β	Angle between vector *a* and *c* in the unit cell
γ	Angle between vector *a* and *b* in the unit cell
V	Volume of unit cell
Z	Number of molecules in the unit cell
Z'	Number of molecules the asymmetric unit of the unit cell
d_{calc}	Calculated density
APC	Atomic packing coefficient
μ	Absorption coefficient
GOF	Goodness-of-fit on F^2
API	Active Pharmaceutical Ingredient
$\Delta_r G°_m$	Standard molar Gibbs of reaction
$\Delta_r H°_m$	Standard molar Enthalpy of reaction
$\Delta_r S°_m$	Standard molar Entropy of reaction
THC	Tramadol hydrochloride
CEL	Celecoxib
IPA	Isopropanol
DMSO	Dimethyl sulfoxide
CTC	Celecoxib:tramadol·HCl cocrystal
PM	Physical mixture
TG	Thermogravimetry

DSC	Differential Scanning Calorimetry
HSM	Hot Stage Microscopy
TAM	Thermal Activity Monitor
m	Mass
M	Molar mass
A	Area of the curve corresponding to the dissolution process
A_b	Area of the curve corresponding to the crucible drop
ε	Energy equivalent of the calorimeter
V	Potential difference
I	Current of intensity
t	Time
Q	Amount of heat
A_c	Area of the calibrated curve
HPLC	High performance liquid chromatography
CTC(SD)	CEL and THC cocrystal produced trough CO_2-assisted nano-spray drying
COA300	CEL and THC coamorph produced trough CO_2-assisted nano-spray drying (particle size 300 nm)
COA900	CEL and THC coamorph produced trough CO_2-assisted nano-spray drying (particle size 900 nm)
SEM	Scanning electron microscopy
T_{on}	Temperature onset
$\Delta_{fus}H_m$	Standard molar fusion enthalpy
$\Delta_{sol}H°_m$	Standard molar enthalpy of solution
$T_{m,A}$	Melting temperature of A
$T_{m,CEL+THC}$	Melting temperature of the PM
$C^s_{p,A}$	cocrystal/coamorph heat capacity
$C^s_{p,CEL}$	CEL heat capacity
$C^s_{p,THC}$	THC heat capacity
$C^l_{p,A}$	molten cocrystal/coamorph heat capacity
$\Delta_{fus+mix}H_m$	Sum of enthalpy of mixing and fusion of a PM
$\Delta_{diss}G$	Gibbs energy of dissolution
R	Ideal gas constant
K_{diss}	Dissolution equilibrium constant
a	Stoichiometric coefficient
n_{CEL}	Amounts of substance of CEL
n_{THC}	Amounts of substance of THC
x_{CEL}	Mole fraction of CEL in equilibrium with the cocrystal
x_{THC}	Mole fraction of THC in equilibrium with the cocrystal
x'_{CEL}	Mole fraction of CEL
x'_{THC}	Mole fraction of THC

Chapter 1

Competition between Halogen and Hydrogen Bonds

1.1 Introduction

Historically, chemistry has been progressing faster and faster to accomplish a higher degree of control of how molecules can be built and interact with other molecules. Nowadays we can synthesize almost any molecule we can think of and are now delving deeper and deeper into how molecules interact, trying to control weaker interactions that, by consequence, are much harder to control.

The prime example of an intermolecular interaction is the hydrogen bond (HB), known for over a century and ubiquitous to life on earth and most of the chemical processes we know. Together with electrostatic and van der Waals interactions, HB are the most well-known interactions. However, in the XIX century several adducts, that seemed to include an attractive interaction between a bonded halogen atom and an electron donor species (usually a carbon or nitrogen), which didn't correspond to any of the previously known interactions, were found.[1] In 1954 Hassel and coworkers determined the crystal structure of one of these adducts and concluded that the halogen atom pointed directly to the electron donor atom.[2] Latter Bent stated that "there is reason to believe that the O···Br-Br interaction is energetically comparable to a strong hydrogen bond",[3] although at the time the interaction was not understood because halogen atoms were considered electron donors, and not electron withdrawing, species. Only at the end of the XX century did we start to uncover the nature of this interaction through *ab initio* calculations by Politzer and coworkers.[4] They found that the covalent bond formed by the halogen atom (X) withdraws electron density from the antibonding orbital at the opposite side of X and creates a very localized area of electron deficiency, the so-called σ-hole. This enables the attractive interaction of the halogen atom with an electron donor group (B) through electrostatic interaction and electron density donation, the now called Halogen Bond (XB), represented in Figure 1.1.

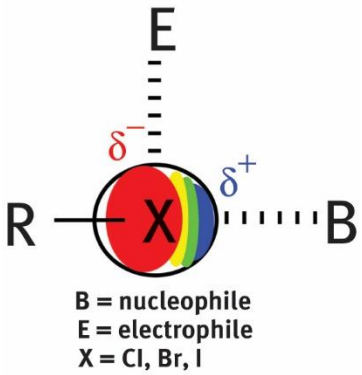

Figure 1.1. Schematic representation of an R–X···B halogen bond showing the anisotropic distribution of charge around the X atom. A possible orthogonal side-on interaction with an electrophile is also shown. The color scheme represents electron density with blue being lower electron density (corresponding to the σ-hole) and red higher electron density.[5]

The properties of XB are similar to HB, namely in terms of directionality, electrostatic and charge-transfer nature, and strength. However XB has additional levels of control possible, such as:[6] (*i*) changing the halogen atom leads to a change in bond strength, increasing with the increase of the atomic weight of the halogen, i.e. F < Cl < Br < I (fluorine atoms are rarely able to form XB[7]), due to the increase in polarizability and electropositivity; (*ii*) the ability of the halogen atom to also behave as an electron donor group; (*iii*) the ability to form bonds with other halogen atoms

in two different kinds of geometry, the so called type I and type II[8] (Figure 1.2). Like HB, the nature of the substituent groups close to the halogen atom in XB has a large influence on the strength of the halogen bond interaction (electron-withdrawing groups will pull electron density from the halogen atom and intensify the σ-hole).

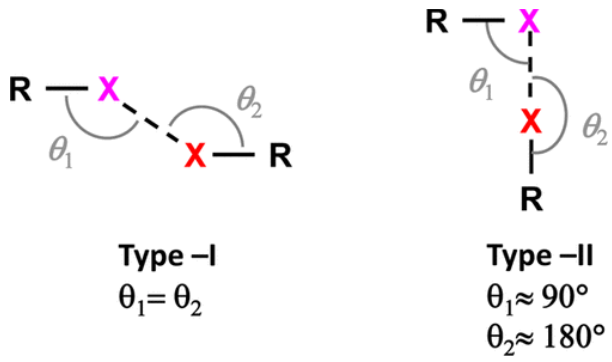

Figure 1.2. Scheme of type I (left) and type II (right) halogen-halogen short contacts. X = halogen, and R = C, N, O, halogen, etc.[6]

The discovery of XB provided a new tool for the development of new compounds and opened a world of possibilities for the expansion of the interaction toolbox that can be used for engineering new materials. Moreover, the development of computational methods, such as quantum chemical and molecular dynamics, has benefited from knowledge of new intermolecular interactions and has returned with new knowledge of XB such as its nature.

Owing to the relatively new studies on XB, the available information on this type of interaction is scarce, when compared with other intermolecular interactions. Moreover, since XB and HB donors can interact with the same electron donor groups, a more in-depth knowledge of how these interactions compete and cooperate has become necessary to achieve a high level of control. A good way to tackle this issue is the systematic search of new compounds that can exhibit both XB and HB, and investigate their relation in terms of cooperation, competition, or both. With sufficient information on this competition/cooperation it is possible to identify patterns and improve the ability to control the conjugation of HB and XB. Examples of HB vs. XB structure screening can already be found in the literature.[9–18]

This work was mainly focused on HB/XB competition and cooperation. The acceptor molecules chosen were 1,4-diazabicyclo[2.2.2]octane (DAB), pyrazine (PYR), both with 2 acceptor sites, and hexamethylenetetramine (HMT) with 4 acceptor sites (Figure 1.3). For the XB/HB donor molecules halogenophenols, changing both halogen atom and substituents relative position, and para substituted dihalogenbenzenes, changing both halogen atoms, were chosen (Figure 1.3). The XB/HB donor molecules were halogenophenols, differing in the halogen atoms and their positions in the aromatic ring, and para substituted dihalogenbenzenes, containing two different halogen atoms (Figure 1.3). The halogenophenol donors allowed the study of the effect of changing both the relative position and the halogen atom. The effect of varying the halogen substituent on the XB strength has been computationally addressed,[19] but to the best of our knowledge, no experimental studies on this topic exist. The para substituted dihalogenbenzenes donor molecules cannot form HB. They were therefore also studied in this work to evaluate their ability to form halogen bonds with the acceptor molecules, without competition from HB.

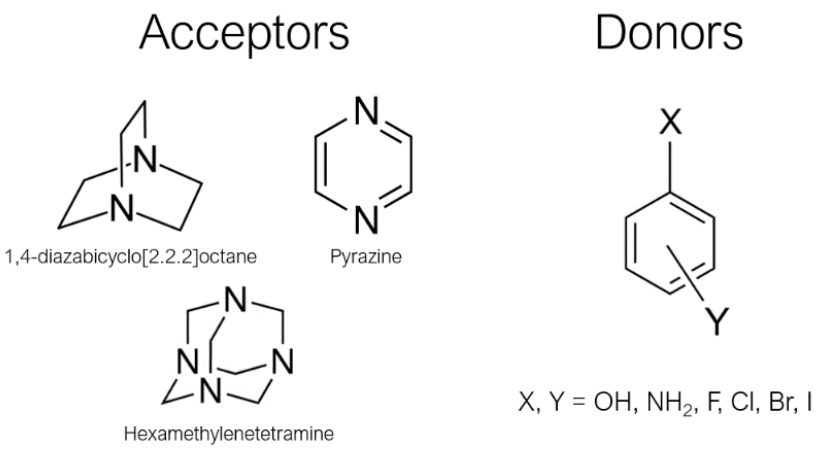

Figure 1.3. Molecular structures of the compounds studied in this work.

1.2 Materials and Methods

Materials

Dichloromethane (DCM, LAB-SCANDCM, 99.8%), Hexane (Sigma-Aldrich, >99%), Pyrazine (PYR, ThermoScientific, >99%), hexamethylenetetramine (HMT, TCL, >99.0%), 1,4-diazabicyclo[2.2.2]octane (DAB, TCL, >98%), 4-fluorophenol (4FP, AmBeed, 99.93%), 2-chlorophenol (2CP, TCL, >99.0%), 4-chlorophenol (4CP, Sigma-Aldrich, ≥99.0%), 2-bromophenol (2BP, TCL, >98%), 3-bromophenol (3BP, TCL, >95%), 4-bromophenol (4BP, Sigma-Aldrich, 99%), 2-iodophenol (2IP, Sigma-Aldrich, 98%), 4-iodophenol (4IP, Sigma-Aldrich, 99%), 4-iodoaniline (4IA, AmBeed, 99.65%), 1-fluoro-4-iodobenzene (1F4IB, AmBeed, 99.87%), 1,4-diiodobenzene (1I4IB, AmBeed, 99.87%), 1-bromo-4-iodobenzene (1B4IB, AmBeed, 98%), 1,4-dibromobenzene (1B4BB, AmBeed, 99.85%), 1-bromo-4-chlorobenzene (1B4CB, AmBeed, 99.92%), 1-chloro-4-iodobenzene (1C4IB, AmBeed, 99.87%) were used as received. 3-Chlorophenol (3CP, Sigma-Aldrich, 98% HPLC) was purified by sublimation.

Cocrystal Synthesis

Cocrystal screening was performed by mechanochemistry using a vibration ball mill (Pulverisette 23, Fritsch). Typically, a stoichiometric mixture of 2 parts Lewis acid to 1 part base (200 mg total mass) was ground for 30 min at a frequency of 50 Hz, inside a 10 cm^3 stainless steel jar containing two 10 mm diameter stainless steel balls. The resulting product was stored at room temperature (298 ± 2 K) in an Eppendorf tube.

Single crystals were produced through slow crystallization of a solution in a mixture of DCM and hexane. In a typical crystallization 30 mg of cocrystal produced through mechanochemistry were dissolved in a mixture of 0.5 mL DCM and 2 mL hexane. If the product did not fully dissolve, an additional 0.5 mL of DCM was added. The solution was allowed to evaporate at 298 ± 2 K until crystal formation was observed. The crystallizations were performed using new and clean 5 mL vials.

Powder X-Ray Diffraction (PXRD)

PXRD patterns were collected at 295 ± 2 K, on a Philips X'Pert PRO X-ray diffractometer operating in the θ-2θ mode. The apparatus was equipped with a PW 3050/60 vertical goniometer, an X'Celerator detector, and a Cu Kα radiation source, with tube amperage and voltage set to 30 mA and 40 kV, respectively. The diffractograms were recorded in the 2θ range 5-35°, in the continuous mode, with a step size of 0.017°(2θ) and an acquisition time of 20 s per step. The samples were mounted on a silicon sample holder. Mercury 2022.3.0 (Build 364735)[20] was used to simulate diffraction patterns from published single crystal X-ray diffraction data.

Single-Crystal X-Ray Diffraction (SCXRD)

Single-crystal X-ray diffraction analysis was carried out by Inês Feliciano and Professor Fátima Piedade at the IST X-ray diffraction facility. They were carried at 296 ± 2 K, on a Bruker AXS-KAPPA APEX II area detector diffractometer, using graphite-monochromated MoKα (λ = 0.71073 Å) radiation. The crystals were coated with Paratone-N oil and mounted on a Kaptan loop. The temperature scale of the apparatus had been previously calibrated against a standard platinum resistance thermometer (calibrated at an accredited facility in accordance with the

International Temperature Scale ITS-90) placed at the same position as the crystal. The X-ray generator was operated at 50 kV and 30 mA, and the X-ray data collection was monitored with the APEX2 program.[21] All data were corrected for Lorentzian, polarization, and absorption effects using the SAINT[21] and SADABS[21] programs. The structures were solved by direct methods with SHELXS-97[22] and refined by full-matrix least-squares on F2 with SHELXLv.2017,[23] included in WINGX-Version 1.80.05.[24] Non-hydrogen atoms were refined with anisotropic thermal parameters. All hydrogen atoms were located in a Fourier map, and their positions and isotropic displacement parameters, Uiso(H), were refined freely. A summary of the crystal data, structure solution, and refinement parameters is given in Table 1.1. Graphical representations were prepared using Mercury 2022.3.0 (Build 364735).[20]

Quantum Chemical Calculations

DFT calculations were performed with the M06-2X functional[25] and the polarized triple-ζ def2-TZVP basis set.[26] This model has been shown to be accurate for treating noncovalent bonds such as those studied here.[19] The computations were carried out with Gaussian 09 program.[27] Before the interaction energy determination, a tight optimization of the geometry was performed. The interaction energy E_{int} of each dimer was calculated as the difference between the electronic energy of the full complex and the sum of the electronic energies of the Lewis acid and the base at absolute zero, each in the geometry they adopt within the dimer. The counterpoise procedure[28,29] was applied to correct basis set superposition error of the electronic interaction energy, E_{int}.

Reactions Monitored *In Situ* and Real Time by Synchrotron PXRD

The experiments were carried out in collaboration with Franziska Emmerling's group (BAM, Berlin) at the μ-spot beamline (BESSY II, Helmholtz Centre Berlin for Materials and Energy, Germany).[30,31] The reactions were performed in a vibration ball mill (Pulverisette 23, Fritsch) at a frequency of 50 Hz and 315 ± 1 K. A Perspex milling jar (internal diameter of 12 mm and wall thickness of 0.75 mm) was used with two 8 mm stainless-steel balls. The experimental setup had been previously described.[32] The experiments were conducted with a wavelength of 0.7293 Å (17 keV) using a double crystal monochromator (Si 111) and a Eiger 9 M (Dectris, Switzerland) detector. PXRD patterns were collected with an acquisition time of 5.75 ± 0.05 s each. Scattering images were integrated using the Dpdak-Software.[33] Data analysis was performed with a custom-made python script.

Table 1.1. Crystal Data and Structure Refinement Parameters

	3CP$_2$:DAB	***3BP$_2$:DAB***	***4IP$_2$:DAB***	***4CP$_2$:HMT***	***4BP$_2$:HMT***	***4IP$_2$:HMT***
T /K	298 ± 2	298 ± 2	293 ± 2	298 ± 2	298 ± 2	298 ± 2
Crystal size /mm	0.30 × 0.15 × 0.10	0.30 × 0.12 × 0.10	0.40 × 0.05 × 0.02	0.40 × 0.03 × 0.02	0.42 × 0.06 × 0.03	0.20 × 0.10 × 0.09
crystal system	Monoclinic	Monoclinic	Monoclinic	Monoclinic	Monoclinic	Monoclinic
space group	P 2_1/c	P 2_1/c	P 2_1/n	P 2_1/c	P 2_1/c	P 2_1/c
a /Å	15.8034(9)	15.8107(16)	6.6265(6)	16.2550(14)	16.372(3)	5.8855(6)
b /Å	9.5503(5)	9.5204(10)	19.238(2)	5.8917(4)	5.8968(9)	13.0647(15)
c /Å	13.3587(7)	13.7718(15)	16.2787(16)	20.6480(15)	21.002(3)	26.755(3)
α /°	90	90	90	90	90	90
β /°	111.713(2)	112.339(3)	90.159(4)	94.210(2)	93.945(6)	92.768(3)
γ /°	90	90	90	90	90	90
V /Å^3	1873.14(18)	1917.4(4)	2075.2(4)	1972.1(3)	2022.8(5)	2054.9(4)
Z	4	4	4	4	4	4
Z'	0	0	0	0	0	0
d_{calc} /g·cm^{-3}	1.309	1.587	1.767	1.338	1.597	1.875
APC	0.694	0.660	0.634	0.651	0.653	0.664
μ /mm^{-1}	0.359	4.240	3.043	0.349	4.027	3.080
F(000)	776	920	1064	832	976	1120
θ limits /deg	2.544 to 26.741	2.553 to 26.421	2.459 to 26.393	2.264 to 27.138	2.381 to 26.381	2.180 to 27.116
limiting indices	-19≤h≤19 -12≤k≤12 -16≤l≤16	-19≤h≤19 -11≤k≤11 -17≤l≤17	-8≤h≤7 -24≤k≤24 -20≤l≤20	-20≤h≤20 -7≤k≤7 -26≤l≤26	-20≤h≤20 -7≤k≤7 -26≤l≤25	-7≤h≤7 -16≤k≤16 -34≤l≤34
reflections collected /unique	27478 / 3974 [R(int) = 0.0496]	42408 / 3915 [R(int) = 0.0914]	49297 / 4253 [R(int) = 0.0818]	29282 / 4368 [R(int) = 0.1107]	18912 / 4042 [R(int) = 0.0811]	49057 / 4564 [R(int) = 0.0777]
completeness to °θ	100.0%	99.9%	99.9%	99.7%	97.4%	99.9%
data/restraints/parameters	3974 / 0 / 360	3915 / 0 / 218	4253 / 0 / 217	4368 / 0 / 243	4042 / 0 / 243	4564 / 0 / 235
GOF on F^2	1.050	1.014	1.055	1.070	1.081	1.151
final R indices [I > 2σ(I)]	R_1 = 0.0594, wR_2 = 0.1363	R_1 = 0.0416, wR_2 = 0.1104	R_1 = 0.0501, wR_2 = 0.1114	R_1 = 0.0777, wR_2 = 0.1209	R_1 = 0.0547, wR_2 = 0.1262	R_1 = 0.0490, wR_2 = 0.0924
R indices (all data)	R_1 = 0.0957 wR_2 = 0.1518	R_1 = 0.0805 wR_2 = 0.1247	R_1 = 0.0759 wR_2 = 0.1189	R_1 = 0.1427 wR_2 = 0.1382	R_1 = 0.1169 wR_2 = 0.1403	R_1 = 0.0633 wR_2 = 0.0976
largest diff. peak and hole ×10^6/e·pm^{-3}	0.287 and -0.348	0.671 and -0.679	1.757 and -0.979	0.357 and -0.320	0.541 and -0.885	0.941 and -0.812

1.3 Results and Discussion

Cocrystal Screening

An initial cocrystal screening using all possible linear combinations of PYR, DAB and HMT (Figure 1.3) with 4FP, 2CP, 3CP, 4CP, 2BP, 3BP, 4BP, 2IP, 4IP, 4IA, 1B4BB, 1B4CB, 1F4IB, 1C4IB, 1B4IB and 1I4IB (Figure 1.4) was performed. The mechanochemical experiments were carried out without solvent assistance, as described in the experimental section. Only one stoichiometric composition was tested: 2 molecular equivalents of the donor molecule to one molecular equivalent of the acceptor molecule. The product of the reaction was analyzed using PXRD and the obtained patterns compared with those of the precursors to confirm if the cocrystal synthesis had been successful. To the best of our knowledge only 3 of the combinations tested had already been shown to produce a cocrystal: $4CP_2$:DAB (2:1, CSD refcode: WIDNAZ[34]), $4BP_2$:DAB (2:1, CSD refcode: WIDNED[34]) and $4IP_2$:DAB (2:1, CSD refcode: IXUVUU[10]). The results are summarized in Table 1.2. The comparisons of the PXRD patterns of the products and precursors are illustrated in Figures S1-S39 of the Supplementary Information.

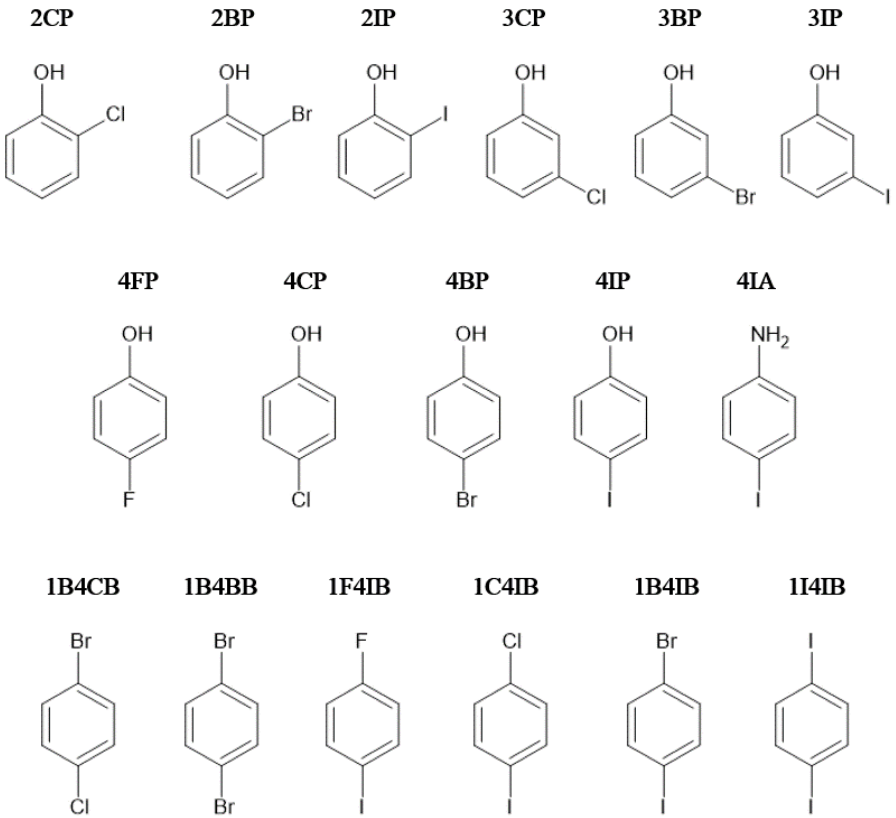

Figure 1.4. Molecular structure of the halogen bond and hydrogen bond donors selected in this work.

Table 1.2. Cocrystal screening sumary. The symbols represent unsuccessful synthesis (-), successfull synthesis (+) and successful preexisting synthesis (○). The highlighted cells mark the products for which structures were determied in this work.

	PYR	DAB	HMT
4FP	-	+	+
2CP	-	-	+
3CP	-	+	+
4CP	+	○[34]	+
2BP	-	+	+
3BP	-	+	+
4BP	+	○[34]	+
2IP	-	+	+
4IP	+	○[10]	+
4IA	-	+	-
1B4BB	-	+	-
1B4CB	-	-	-
1F4IB	-	+	-
1C4IB	-	+	-
1B4IB	-	+	+
1I4IB	-	+	+

Most of the synthesis with PYR produced a liquid, and some mixtures liquified upon mixing, even without milling. Almost all reactions with DAB and HMT were successful. The cocrystal products that had already been published, or were determined in this work, had matching structures, as can be confirmed by the PXRD results represented in Figure S 1 to Figure S 39 of the Supplementary Information.

Structures

The results of the SCRXD experiments indicated that all synthesized products corresponded to cocrystals with 2:1 stoichiometry, two equivalents of the donor molecule to one equivalent of acceptor molecule.

Table 1.3. Structural data of the determined crystal structures.

	3CP$_2$:DAB	***3BP$_2$:DAB***	***4IP$_2$:DAB***	***4CP$_2$:HMT***	***4BP$_2$:HMT***	***4IP$_2$:HMT***
d (O···N)$_1$ /Å	2.674	2.718	2.654	2.745	2.743	2.743
d (O···N)$_2$ /Å	2.715	2.671	2.699	2.764	2.756	2.808
∠ (C···O···N)$_1$ /°	121.48	120.08	124.00	118.76	118.57	113.29
∠ (C···O···N)$_2$ /°	120.06	121.09	119.33	118.32	119.03	113.85
d (X···N) /Å	-	-	-	-	-	3.040
∠ (C···X···N) /°	-	-	-	-	-	172.78

3CP$_2$:DAB

The asymmetric unit of 3CP$_2$:DAB cocrystal is represented in Figure 1.5a. It shows 3 symmetry independent molecules, 2 donor molecules and one acceptor molecule. The structure reveals that both acceptor sites are bonded with an HB with distances O···N of 2.674 Å and 2.715 Å. The chlorine atoms do not form halogen bonds: one is directed to the hydroxyl carbon of another 3CP molecule (Figure 1.5b) with a C···X distance of 3.478 Å and another is directed to an hydrogen of

a second 3CP molecule with a H···X distance of 3.003 Å. The three-dimensional packing is composed of stacked molecular layers (Figure 1.5c represents a molecular layer). The two asymmetric molecules of 3CP can be seen in this representation: one of the molecules alternates with DAB in an orthogonal direction to the ring plane (top highlight in Figure 1.5c); the second asymmetric 3CP molecule forms rows of alternating direction (bottom highlight in Figure 1.5c). The DAB molecule shows disorder with rotation with the axis of rotation being the two nitrogen atoms.

3BP$_2$:DAB

The structure of 3BP$_2$:DAB shows the same molecular packing of 3CP$_2$:DAB (Figure 1.6). The hydrogen bond O···N distances are 2.718 Å and 2.671 Å. The halogen atoms show a C···X distance is 3.431 Å and a H···X distance of 3.156 Å in the same motifs as 3CP$_2$:DAB. The structure also consists also of stacked layers (Figure 1.6c) with the same molecular motifs as 3CP$_2$:DAB.

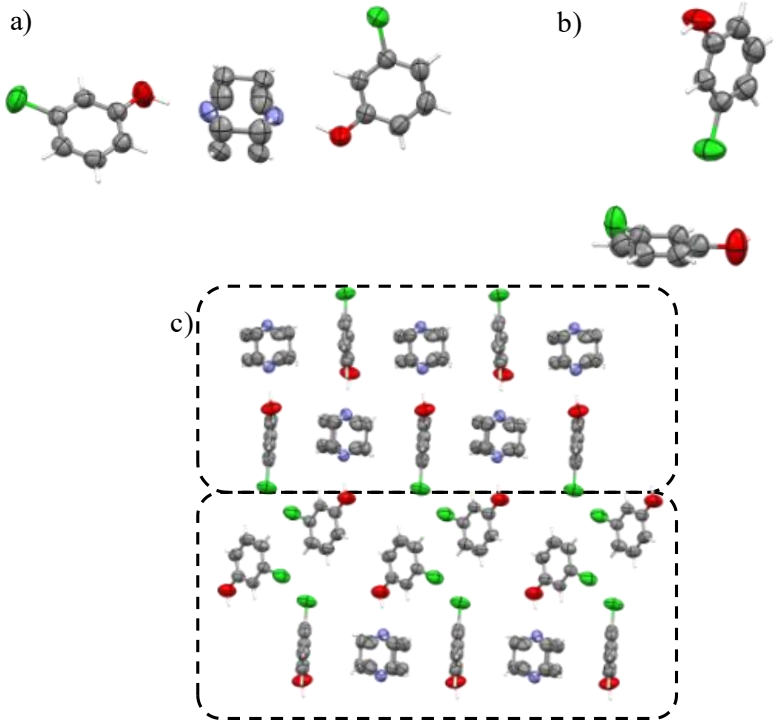

Figure 1.5. Main packing motifs of 3CP$_2$:DAB cocrystal. a) asymmetric unit, b) chlorine-pi interaction, c) three-dimensional packing motif with the highlight of the two packing motifs.

4IP$_2$:DAB

The structure of the 4IP$_2$:DAB had been previously reported (CSD refcode: IXUVUU, also determined at room temperature, 283-303 K). Despite this, one of the hydrogen atoms in the hydroxyl group did not seem to be correctly positioned. The structure determined in this work matched the literature structure and presented two hydrogen bonds with O···N distances of 2.654 Å and 2.699 Å. The iodine atoms participate in an interesting supramolecular arrangement of 3 halogen bonds (Figure 1.7b), the arrangement is composed of two XB of type I (I···I distances of 3.836 Å, I···I···C angles of 125.94°) and one XB of type II (I···I distance of 3.796 Å, I···I···C angle of 153.76°). The three-dimensional packing of the molecules consists of stacked 4IP and DAB rows with the iodine atoms pointing at each other forming linear channels, marked in green, in the structure (Figure 1.7c).

4CP$_2$:HMT

The 4CP$_2$:HMT asymmetric unit includes two 4CP molecules and one HMT molecule. The HMT molecule forms two HB with the 4CP molecules with O···N distances of 2.745 Å and 2.764 Å (Figure 1.8a). The chlorine atoms interact with CH···Cl HB with HMT (Figure 1.8b) showing a distance H···Cl of 3.155 Å. The three-dimensional arrangement consists of stacked chains of each molecule (Figure 1.8c).

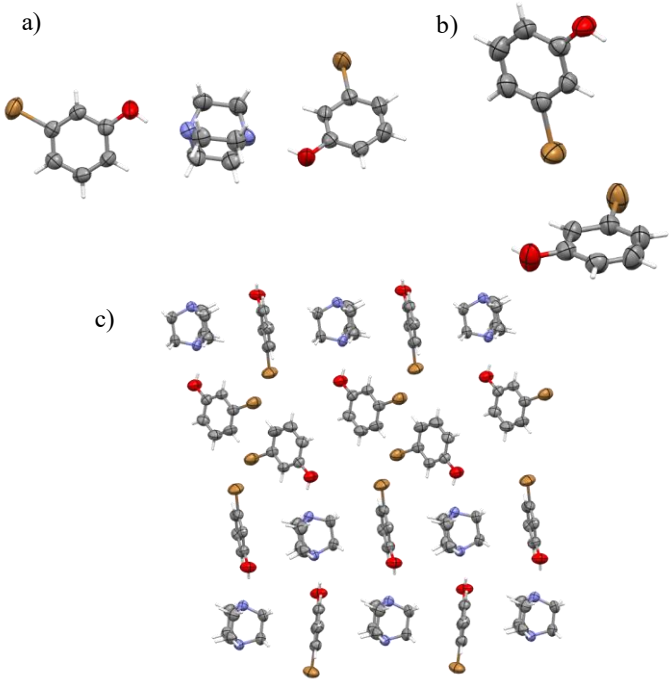

Figure 1.6. Main packing motifs of 3BP$_2$:DAB cocrystal. a) asymmetric unit, b) bromine-pi interaction, c) three-dimensional packing motif.

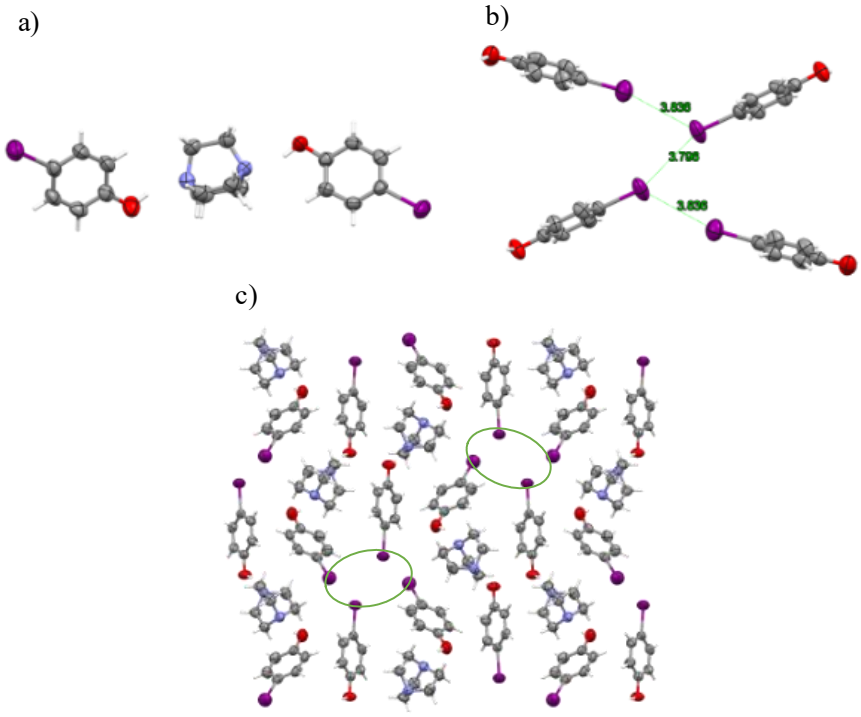

Figure 1.7. Main packing motifs of 4IP$_2$:DAB cocrystal. a) asymmetric unit, b) iodine-iodine interactions, c) three-dimensional packing motif.

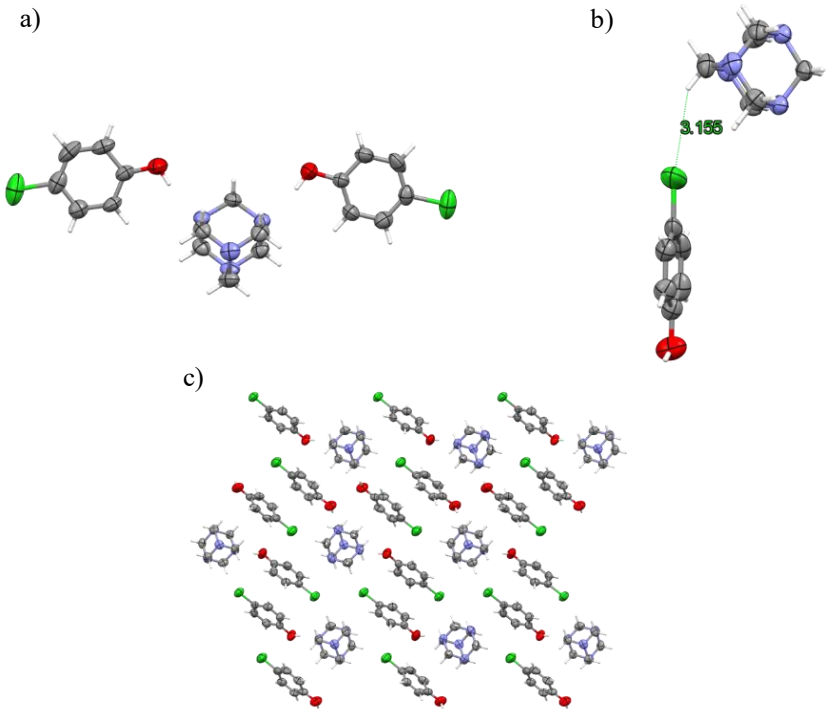

Figure 1.8. Main packing motifs of $4CP_2$:HMT cocrystal. a) asymmetric unit, b) chlorine-hydrogen interaction, c) three-dimensional packing motif.

$4BP_2$:HMT

The $4BP_2$:HMT cocrystal packing is similar to that of $4CP_2$:HMT. The asymmetric unit is composed of two 4BP molecules which form hydrogen bonds with HMT with O···N distances of 2.743 Å and 2.756 Å (Figure 1.9a). The CH···X interaction seen in $4CP_2$:HMT is also present in this case with a CH···Br distance of 3.332 Å (Figure 1.9b). The three-dimensional arrangement is also composed of stacked chains of each molecule (Figure 1.9c).

$4IP_2$:HMT

The $4IP_2$:HMT cocrystal presents the only structure where halogen bonds with the acceptor were found. The asymmetric unit is still only composed by two 4IP molecules forming hydrogen bonds with HMT with distances of 2.743 Å and 2.808 Å (Figure 1.10a). One of the iodine atoms participates in a halogen bond with HMT with a N···I distance of 3.040 Å (Figure 1.10b). The second iodine atom is pointing to a hydrogen atom of HMT with a CH···I distance of 3.200 Å. The three-dimensional arrangement is also composed of stacked chains of each molecule (Figure 1.10c).

Quantum Chemical Calculations

The interaction energy and bond distances between the halogenophenols and DAB for an isolated adduct in the gas phase were determined using DFT. Fluorine dimers were not considered because they do not form halogen bonds. This was confirmed because calculations with such types of dimers did not converge to geometries compatible with halogen bond interactions.

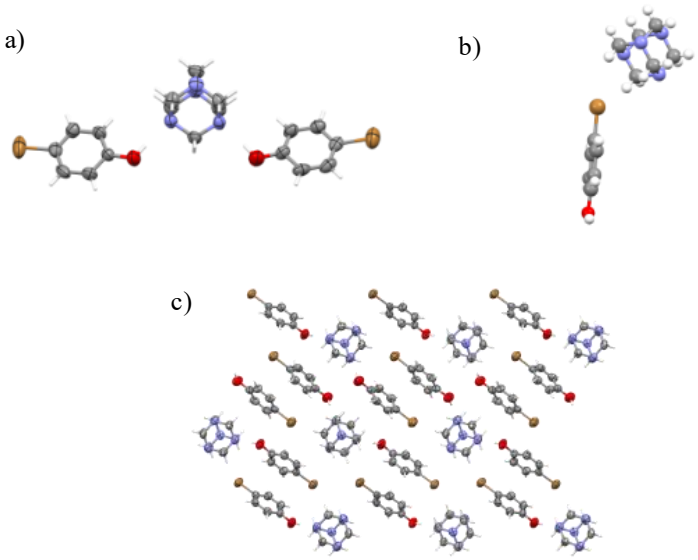

Figure 1.9. Main packing motifs of $4BP_2$:HMT cocrystal. a) asymmetric unit, b) bromine-hydrogen interaction, c) three-dimensional packing motif.

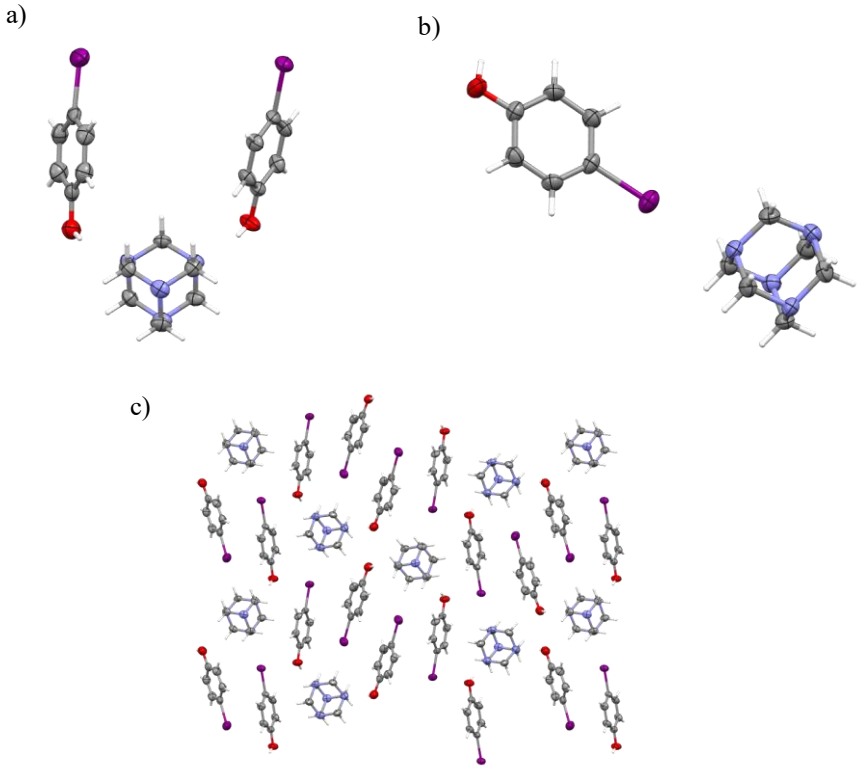

Figure 1.10. Main packing motifs of $4IP_2$:HMT cocrystal. a) asymmetric unit, b) halogen bond interaction, c) three-dimensional packing motif.

The results are summarized in Table 1.4 and illustrated in Figure 1.11. The interaction energies are expressed as dissociation energies ($-E_{int}$) so that higher values correspond to stronger intermolecular bonds. From these results it can be concluded that:

(i) HB are the strongest interactions ($60 < -E_{int} < 67$ kJ·mol^{-1}) followed by the XB with the nitrogen acceptor ($10 < -E_{int} < 30$ kJ·mol^{-1}), and halogen-halogen bonds ($1.7 < -E_{int} < 7$ kJ·mol^{-1}).

(ii) The N···X halogen bonds are the most sensitive to the change in halogen atom with differences amounting up to 16 kJ·mol^{-1}. Despite HB showing higher absolute sensitivity to the nature of the halogen, X···X show a much higher relative change in $-E_{int}$, as the E_{int} for X···X dimers more than triplicates along the series chlorine, bromine, iodine.

(iii) The change in relative position of the hydroxyl group and the halogen atom changes the $-E_{int}$ value. As the substituents get closer in the ring, the $-E_{int}$ value becomes higher for all types of interaction. This change is, however, more pronounced going from the meta to the ortho substituted rings than from the para to the meta substituted rings (see Table 1.4).

The results for the bond distances reveal similar trends as E_{int}. Indeed, the bond distance results suggest that:

(i) The hydrogen bonds have the smallest bond distances ($2.697 < d_{O\cdots N} < 2.723$ Å) followed by the N···X halogen bonds ($2.967 < d_{X\cdots N} < 3.084$ Å) and finally halogen-halogen bonds ($3.556 < d_{X\cdots X} < 3.846$ Å).

(ii) The halogen-halogen bonds are the most sensitive to the change in halogen atom. This result has, however, to be weighed with the change in the van der Waals radii of the different halogen atoms, which increases by 0.04 Å from chlorine to bromine and by 0.18 Å from bromine to iodine.[35] Nonetheless, the change in halogen atoms produces a higher difference in both $d_{X\cdots N}$ and $d_{X\cdots X}$ than the van der Waals radii difference.

(iii) Changing the relative position of the hydroxyl group and the halogen atom in the donor molecule produces the same trend observed for E_{int}: as the substituents get closer the bond distances get smaller. The exceptions to this trend are the $d_{X\cdots X}$ and $d_{N\cdots X}$ distances for the iodo substituted donor molecules.

Table 1.4. Interaction energies, $-E_{int}$, and interaction distances between halogenophenols-DAB dimers and halogenophenols- halogenophenols dimers.

	$-E_{int}$ /kJ·mol^{-1}			d /Å		
	OH···N	N···X	X···X	O···N	N···X	X···X
4FP	60.99			2.723		
4CP	62.87	10.64	1.73	2.714	3.084	3.558
4BP	63.74	15.60	3.08	2.714	2.997	3.593
4IP	63.69	26.04	6.02	2.717	2.995	3.837
3FP	61.52			2.719		
3CP	63.88	11.12	2.07	2.708	3.004	3.556
3BP	62.92	16.13	3.32	2.708	2.989	3.583
3IP	63.74	27.25	6.16	2.717	2.970	3.841
2FP	64.56			2.702		
2CP	65.57	12.90		2.697	2.977	
2BP	65.95	18.44	4.28	2.688	2.967	3.569
2IP	66.48	29.27	6.98	2.697	2.985	3.846

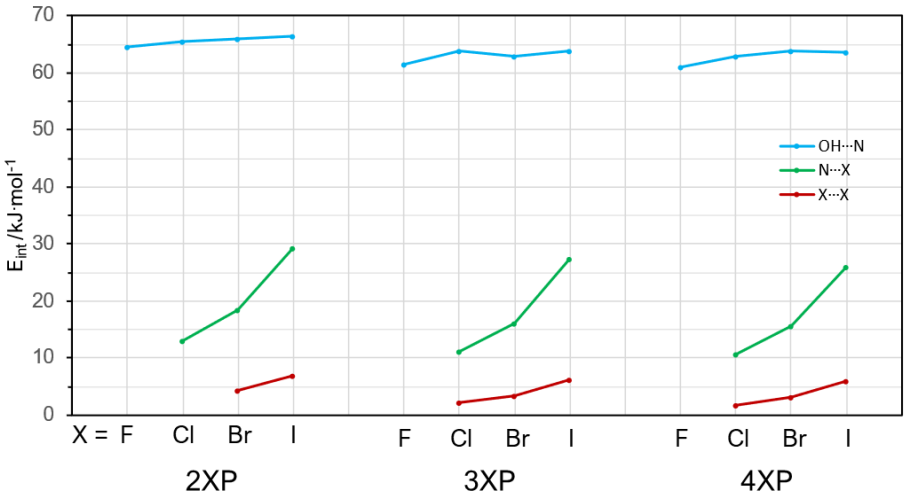

Figure 1.11. Graphical representation of the interaction energies between the halogenophenols and DAB following the different interaction types, OH···N, N···X and X···X

Cocrystal Formation Reactions Monitored *In Situ* and in Real Time by Synchrotron PXRD

The kinetics of the reaction of 4IP and 4BP with DAB were analyzed trough *in situ* synchrotron PXRD (Figure 1.12). The products obtained during these experiments matched the ones previously found in the cocrystal screening. The results show that the kinetics of cocrystal syntheses are very fast: for 4IP:DAB the reaction was complete after 7 scans (~40 s); for 4BP:DAB the reaction was complete after 8 scans (~46 s). Since the reaction times are very short, the obtained data were not sufficient for a quantitative determination of rate constants. These preliminary results were, nevertheless, useful to plan new and more effective experiments to be carried out when beamtime is available. Indeed, the results suggest that an increase in reaction time can be achieved if lower milling frequency and lower temperature are used.

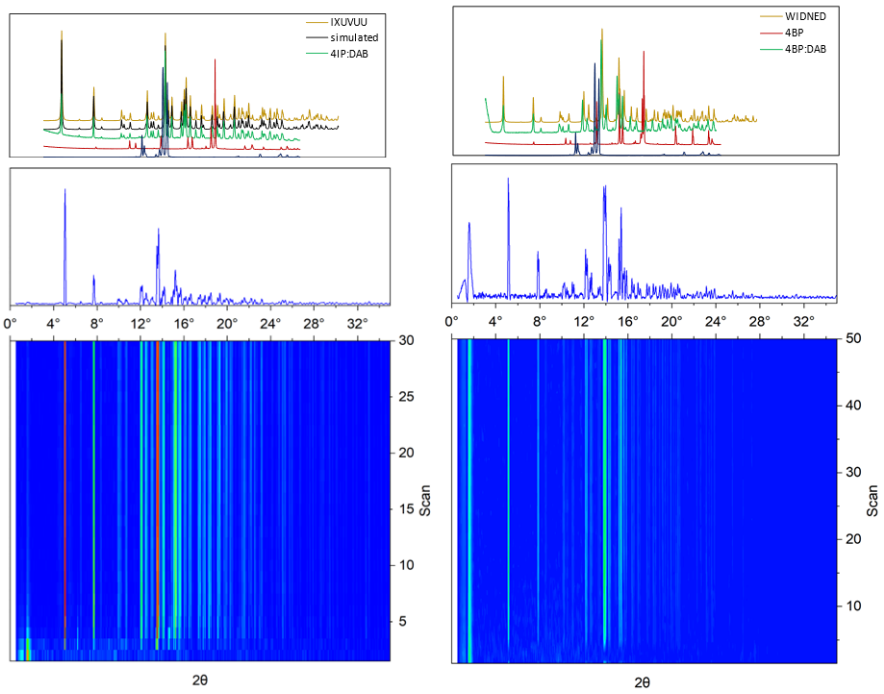

Figure 1.12. In situ real time PXRD of the reaction of 4IP with DAB (left) and 4BP with DAB (right).

1.4 Conclusion

The cocrystal screening, through mechanochemistry, with both HB and XB donor molecules and acceptor molecules resulted in 25 new cocrystals (3 with PYR, 11 with DAB and 11 with HMT) and the replication of 3 previously described cocrystals. A molar ratio of 2 donor molecules to 1 acceptor molecule was used. The structure of 6 of these cocrystals was determined, namely, $3CP_2$:DAB, $3BP_2$:DAB, $4IP_2$:DAB, $4CP_2$:HMT, $4BP_2$:HMT and $4IP_2$:HMT (previously determined). All structures determined revealed that both hydroxyl groups were involved in a HB with the acceptor molecule, while the halogen atom was only involved in a XB with the acceptor in the $4IP_2$:HMT cocrystal. Nonetheless, the $4IP_2$:DAB cocrystal revealed a structural motif with 3 halogen-halogen bonds, namely two of type I and one of type II, despite the main motif being composed of two hydrogen bonds.

The quantum chemical calculations of the interaction energies and bond distances between halogenophenols and DAB showed that:

(i) Dimers involving Fluorine did not form XB.

(ii) HB is the strongest interaction, followed by XB with the acceptor molecule and finally the halogen-halogen bond. The same effect is seen for the bond distances with stronger interactions resulting in smaller bond distances.

(iii) The change of the halogen atom has a higher impact on the strength of the N···X interaction followed by the X···X interaction and finally the hydrogen bonded dimers. Nonetheless the impact on the distance is the highest for the X···X dimers followed by N···X dimers and finally hydrogen bonded dimers.

(iv) Changing the relative position of the hydroxyl group to the halogen atom in a ring has an impact on the strength of all types of interactions with a larger effect being observed on going from meta to ortho than from para to meta substituted molecules. The same trend in seen for bond distances with the exception of the $d_{X\cdots X}$ and $d_{N\cdots X}$ distances for the iodo substituted donor molecules.

The preliminary *in situ* and real time monitoring of cocrystal formation reactions by synchrotron PXRD revealed that the 4IP+DAB and 4BP+DAB systems react both very rapidly (<1 min) in the experimental conditions used.

Chapter 2

On the Stability of Celecoxib-Tramadol·HCl: Cocrystal versus Amorphous Nanoparticles

2.1 Introduction

For a solid oral drug product to reach the market, it must contain an active pharmaceutical ingredient (API) that is both chemically and physically stable and has sufficient solubility in the gastrointestinal tract to enable absorption.[36,37] In view of these prerequisites, many promising drugs never reach the market because of poor bioavailability originated by low solubility. In fact, it has been estimated that about 90% of all compounds in today's pharmaceutical drug delivery pipelines are poorly soluble in water.[38] The efficacy of a drug can, normally, be optimized by changing the API molecular structure or its formulation. Changing the molecular structure is frequently not an option, because it implies the development of a new drug that is costly and time-consuming. For this reason, there is an increasing interest in new and better methods to improve the properties of an API (e.g., solubility) that are critical for achieving an adequate and controllable bioavailability.

Crystal engineering has, over the years, introduced many methods to manipulate the organization of molecules in a solid form, enabling the improvement of solubility and other properties of a compound without changing the structure of the main building unit. Some examples are the formation of cocrystals,[39] salts,[40] nanoparticles,[40,41] metastable polymorphs, and amorphous forms.[42]

Cocrystals have emerged as one of the most promising crystal engineering approaches to improve the properties of functional materials. Due to the practically limitless possibilities of molecular combinations, cocrystals provide a means to tune the properties of functional materials that are relevant for diverse industrial sectors such energetic materials, agrochemicals, and particularly pharmaceuticals. To avoid performance loss and shorter shelf-life, pharmaceutical companies generally avoid commercializing drugs based on metastable forms. Thus, within this scope, cocrystals are generally preferred over nanoparticles, amorphous forms, and metastable polymorphs, because they offer the opportunity to improve both stability and solubility, while in for other approaches solubility increase is often accompanied by a stability decrease. The use of metastable materials requires unequivocal proof that a kinetic barrier hinders their transformation to thermodynamically more stable forms. For this reason, evaluating the thermodynamic and kinetic stability of new APIs and understanding how they can be tuned by various methodologies is a crucial factor for an effective drug development process.

The thermodynamic stability of a cocrystal (AB) relative to decomposition into the precursors (A and B) can be determined from the standard molar Gibbs energy change, $\Delta_r G°_m$, of the reaction:

$$\mathrm{AB(s)} \rightarrow \mathrm{A(s)} + \mathrm{B(s)} \tag{2.1}$$

On thermodynamic grounds the AB cocrystal will be stable if $\Delta_r G°_m > 0$ for reaction (2.1) or, in other words, has no tendency for spontaneous decomposition into the precursors.[43] The opposite is true for $\Delta_r G°_m < 0$. The value of $\Delta_r G°_m$ includes an enthalpic ($\Delta_r H°_m$) and an entropic ($\Delta_r S°_m$) contribution:

$$\Delta_r G^\circ_m = \Delta_r H^\circ_m - T\Delta_r S^\circ_m \tag{2.2}$$

There is evidence, however, that thermodynamic stability is, in most cases, determined by the enthalpic term,[44,45] which reflects only the change in lattice energy of the cocrystal relative to its precursors. This is a relevant aspect when comparisons with theoretical predictions of cocrystal

stability are intended, because computations normally provide the lattice energy difference associated with reaction (2.1), albeit often based on electronic energies at 0 K.

Currently there is limited experimental information regarding stability cocrystals measured in terms of Gibbs energy and its enthalpic and entropic components. In addition, the comparison of the stability of crystalline with amorphous forms or the impact of the particle size on stability are seldom evaluated on thermodynamic grounds. One further aspect is the fact that the lack of experimental information poses a serious limitation for the development and validation of theoretical methods used to study cocrystals and predict their stability.

Recently, a new cocrystal combining the APIs tramadol hydrochloride (THC, used to treat moderate to severe pain) and celecoxib (CEL, an anti-inflammatory drug) was reported,[46] that presented favorable physicochemical properties and dissolution profiles for application in dual therapy.[47] This cocrystal, used for the bimodal treatment of pain, has recently been approved by the FDA and is sold under the tradename Seglentis. Following this work, O'Sullivan et. al.,[48] reported the production of CEL:THC coamorphous and cocrystalline nanoparticles obtained by supercritical CO_2-assisted nano-spray drying. There is, however, no information on the stability of these materials and how it compares to the stability of a cocrystal produced trough crystallization from solution. The change of thermodynamic stability with the particle size has also not been evaluated.

In this work, we studied different methods to produce tramadol hydrochloride and celecoxib cocrystal, employing mechanochemistry, crystallization from solution and crystallization from melt. Subsequently, we analyzed the thermal behavior of the cocrystal samples, including the recently described coamorphous and cocrystalline nanoparticles. The focus was the determination of the thermodynamic stability of these samples, to highlight the effect that these three strategies, cocrystals, amorphization and nanoparticles, have in the thermodynamic stability of the solid forms. This approach allowed us to gain a deeper understanding on how the different strategies to improve the properties of a drug can affect the stability of the different solid forms.

2.2 Materials and Methods

Materials

Tramadol·HCl (THC, Sigma-Aldrich, ≥99.0% HPLC), celecoxib (CEL, Baoji GuoKang Bio-Technology Co. Ltd., 99.7%), isopropanol (IPA, Honeywell, >99.8% GC) and dimethyl sulfoxide (DMSO, ThermoScientific, 99.9%) were used as received. Coamorphous nanoparticles and cocrystalline nanoparticles of CEL and THC were provided by Luis Padrela at the SSPC Research Centre, (Bernal Institute, University of Limerick, Ireland) and stored beside silica beads at 255 ± 2 K.

Note that the calculation of all molar thermodynamic quantities was based on the molar masses M(CEL) = 381.373 g·mol^{-1}, M(THC) = 299.83 g·mol^{-1} and M(CTC) = M(COA) = 681.219 g·mol^{-1}, obtained from the 2013 standard atomic masses recommended by the IUPAC Commission.[49] The assignment of uncertainties according to literature procedures was previously detailed.[50]

Synthesis of Celecoxib:Tramadol·HCl Cocrystal (CTC)

CTC was first obtained by mechanochemistry using a vibration ball mill (Pulverisette 23, Fritsch). Typically, CEL (61.02 mg, 0.16 mmol) and THC (47.97 mg, 0.16 mmol) were ground for 30 min, at 30 Hz frequency, inside a 10 cm^3 stainless steel jar containing two 10 mm diameter stainless steel balls. The experiments were carried out with the addition of 10 μL of isopropanol. The PXRD pattern agrees with the with the previously reported structure of CTC by Almansa et. al..[46]

To produce a larger amount of CTC, crystallization from solution was used. In this case, 353.82 mg (1.18 mmol) of THC and 450.02 mg of CEL (1.18 mmol) were added to 4 mL of IPA with stirring. The solution was heated until complete dissolution and then allowed to slowly cool to 60 °C over ca. 2h. Once at 60 °C the solution was seeded with a small amount of CTC, produced by mechanochemistry, and subsequently allowed to slowly cool to room temperature (ca. 298 K) and further cooled to 0 °C with a cryostat bath. The resulting solid was filtered and vacuum dried for 12h.

The heating of a physical mixture (PM) of CEL and THC to produce CTC was also tested. An equimolar PM was placed on an PXRD aluminum sample holder and characterized by PXRD before and after being heated on a hotplate at 423 K for 5 min.

Powder X-Ray Diffraction (PXRD)

The PXRD experiments were carried out as described in the Powder X-Ray Diffraction (PXRD) section (page 5).

Thermogravimetry (TG)

TG experiments were carried out on a Perkin Elmer TGA7 apparatus. The samples with an initial mass of 5-11 mg were placed in an open platinum crucible and subject to a temperature ramp at 5 K·min^{-1}, in the range 298-773 K. The balance chamber was kept under a nitrogen flow (Praxair 5.0) of 38 cm^3·min^{-1}. The sample purge gas was nitrogen (Praxair 5.0) at a flow rate of 22.5 cm^3·min^{-1}. The mass scale of the instrument was calibrated with a standard 100 mg weight and

the temperature calibration was based on the measurement of the Curie points (T_C) of alumel alloy (Perkin-Elmer, T_C = 427.35 K) and nickel (Perkin-Elmer, 99.99%, T_C = 628.45 K) standard reference materials.

Differential Scanning Calorimetry (DSC)

Differential scanning calorimetry experiments were performed in the range 298-460 K, on a DSC7 from Perkin Elmer. The Pyris V. 7.0.0.0110 software package was used for instrument control and data acquisition. The samples with a mass of 2-5 mg were sealed in aluminum pans and weighed in a Mettler XP2U ultra-microbalance (±0.1 µg precision). All experiments were carried out at a heating rate of 5 K·min^{-1}, under a dynamic nitrogen (Air Liquide N45) atmosphere (30 cm^3·min^{-1} flow rate). The temperature and enthalpy scale of the apparatus were calibrated at the same heating rate by using indium (Perkin Elmer, 99.999%, T_{fus} = 429.75 K, $\Delta_{fus}h°$ = 28.45 J·g^{-1}) and zinc (Perkin-Elmer, 99.999%, T_{fus} = 692.65 K, $\Delta_{fus}h°$ = 107.5 J·g^{-1}).

Hot Stage Microscopy (HSM)

Hot stage microscopy experiments were performed with an Olympus BX51 polarizing optical microscope equipped with a Linkam LNP hot stage and Linkam TMS94 programmable temperature controller. Images were recorded at selected temperatures using a digital Olympus SC30 video camera. The sample was heated from 298 K to 418 K at a heating rate of 15 K·min^{-1}, then cooled to 298 K and heated a second time to 443 K at a rate of 5 K·min^{-1}.

Solution Calorimetry

Enthalpies of solution in DMSO, at 298.15 K, were measured with a LKB 2277 Thermal Activity Monitor (TAM), shown in Figure 2.1. A in-house designed 15.0 cm^3 stainless steel cell equipped with stirring, dissolution and electrical calibration systems was used, schematized in Figure 2.1.[51] Instrument control and data acquisition were performed with the CBCAL 3.0 program. In a typical experiment, 7-14 mg of sample, contained in an aluminum crucible, was weighted in a Mettler XP2U ultra-microbalance (±0.1 µg precision) and placed in the sample holder of the calorimetric cell. Approximately 17 g of DMSO or an appropriate solution were introduced in the cell body and weighed using a Mettler XS 205 balance (±10 µg precision). The cell was assembled and transferred to the thermostat unit. The dissolution process was started by dropping the crucible into the solvent after recording a suitable baseline. The corresponding enthalpy change was calculated from:

$$\Delta_{sol}H^{\circ}_{m} = \frac{M}{m}\varepsilon(A - A_b) \tag{2.3}$$

$$\varepsilon = \frac{Q}{A_c} \tag{2.4}$$

where m and M represent the mass and molar mass of sample, respectively; A is the area of the curve corresponding to the dissolution process; A_b is the contribution to the measured area due to crucible drop; and ε is the energy equivalent of the calorimeter. An average value of A_b was determined by performing several blank experiments where an empty crucible was dropped into the solvent. The energy equivalent of the calorimeter, ε, was obtained from a series of electrical calibrations where a potential difference V was applied to a 22 Ω manganin resistance immersed in the calorimetric liquid, causing a current of intensity I to flow during a pre-selected time t.

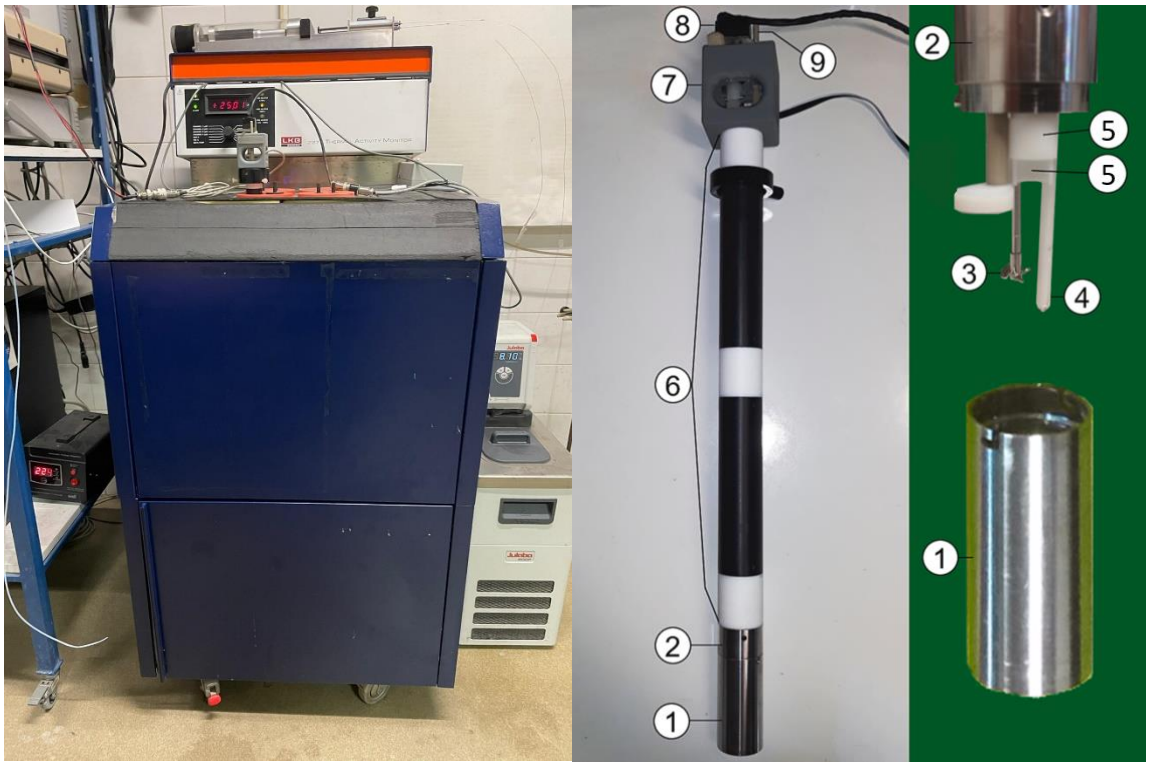

Figure 2.1. LKB 2277 Thermal Activity Monitor (left). Scheme of the calorimetric cell (right): 1 cell vessel; 2 cell lid; 3 stirrer; 4 calibration resistance; 5 sample-drop system; 6 cell body; 7 stirring motor housing; 8 stirring motor; 9 handle that moves the bottom part of the sample-drop system.

This process led to the dissipation of an amount of heat $Q = VIt$ inside the calorimetric cell, reflected by a measured curve of area A_c. The accuracy of the electrical calibration was found to be better than 0.5% by determining the enthalpy of solution of KCl in water.[52]

Solubility Measurements

Solubility was determined by Aaron O'Sullivan at the SSPC Research Centre, University of Limerick. In a typical experiment 200 mg of solid was equilibrated in 4 cm^3 of isopropanol for 24h. After equilibration the excess solid was allowed to settle, and the saturated solution was analyzed by HPLC.

2.3 Results and Discussion

Synthesis of CTC and Coamorphous nanoparticles

The first method to synthesize CTC used ball milling of a THC and CEL physical mixture (PM).[46] The comparison of the PXRD results with the PXRD simulation from the published structure[46] confirms that the product match (Figure 2.2). Nonetheless, the PXRD pattern of the obtained sample shows some small signals due to the precursors, namely at 18° (*2θ)*. These results are expected since ball milling is a highly heterogeneous process. The PXRD pattern for the sample produced through solution crystallization did not show signals from the precursors. Moreover, the signals from this sample showed a higher intensity than the ones from the sample produced by ball milling. This can be an indication of the higher crystallinity of the sample due to larger and/or better crystals.

The heating process of a PM of CEL and THC was investigated to examine the production of CTC. Initially, PXRD of the PM showed a combination of signals from the precursors, however, upon heating to 423 K, there was a change in the sample morphology (Figure 2.3), even though the melting point of the pure compounds or CTC was not reached. After cooling, the PXRD analysis revealed a combination of signals from both the precursors and CTC (Figure 2.2).

The coamorphous samples produced in Ireland trough spray drying showed only amorphous halos in the PXRD pattern, confirming their amorphous nature (Figure 2.2). The cocrystalline sample produced by spray drying showed peaks with a small intensity but corresponding only to the CTC sample, albeit less intense than the cocrystal produced trough solution crystallization. The nanosized samples were also previously analyzed using scanning electron microscopy, SEM.[48] The results, presented in Figure 2.4, show that the amorphous particles present a spheric morphology with no crystal-like features, and confirm the different particle sizes of the two amorphous samples and the needle-like morphology of the crystalline sample. The particle sizes of previously synthesized samples[48] are presented in Table 2.1.

The sample identification codes are as follows:

CTC	CEL and THC cocrystal produced trough crystallization
CTC(SD)	CEL and THC cocrystal produced trough CO_2-assisted nano-spray drying
COA300	CEL and THC coamorph produced trough CO_2-assisted nano-spray drying (particle size 300 nm)
COA900	CEL and THC coamorph produced trough CO_2-assisted nano-spray drying (particle size 900 nm)

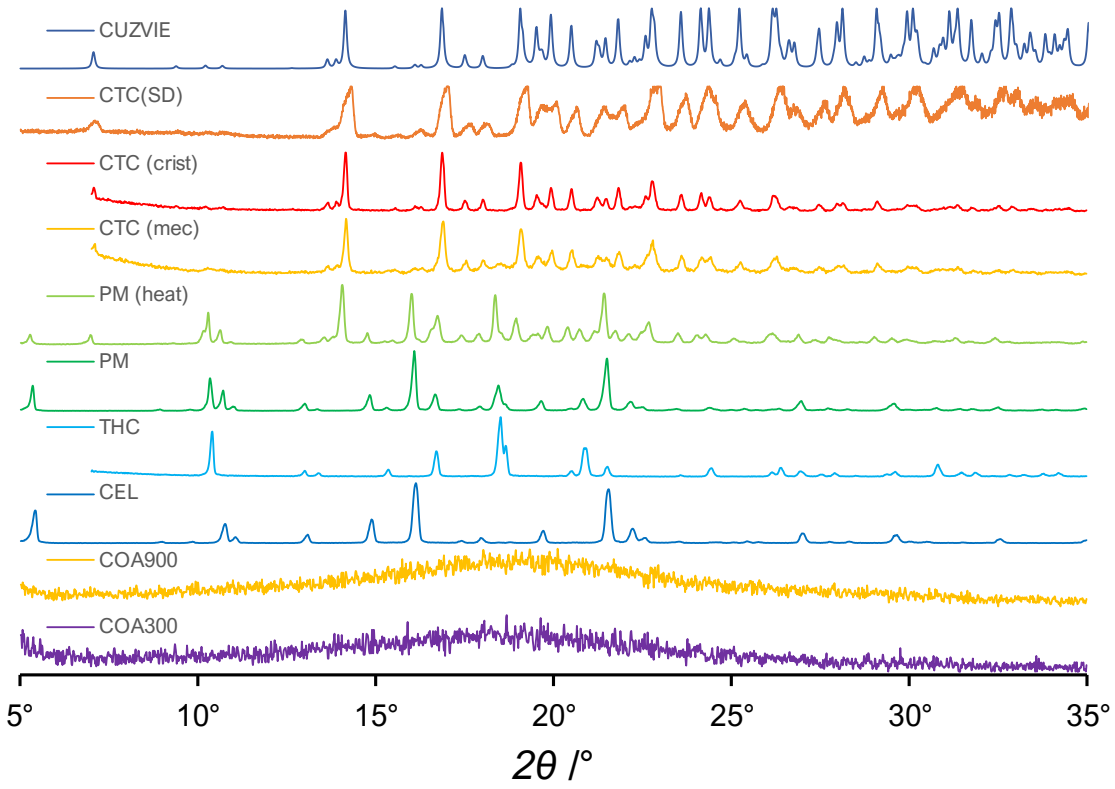

Figure 2.2. Comparison of the PXRD results (normalized intensity values) for CTC produced trough spray drying, CTC(SD), crystallization from solution, CTC(crist), mechanochemistry, CTC(mec), physical mixture (PM), physical mixture after heating to 423 K, PM(heat), THC, CEL, coamorphous samples with particle sizes of 300 nm, COA300, and 900 nm, COA900 and simulated powder pattern from CTC cocrystal structure (refcode:CUZVIE).

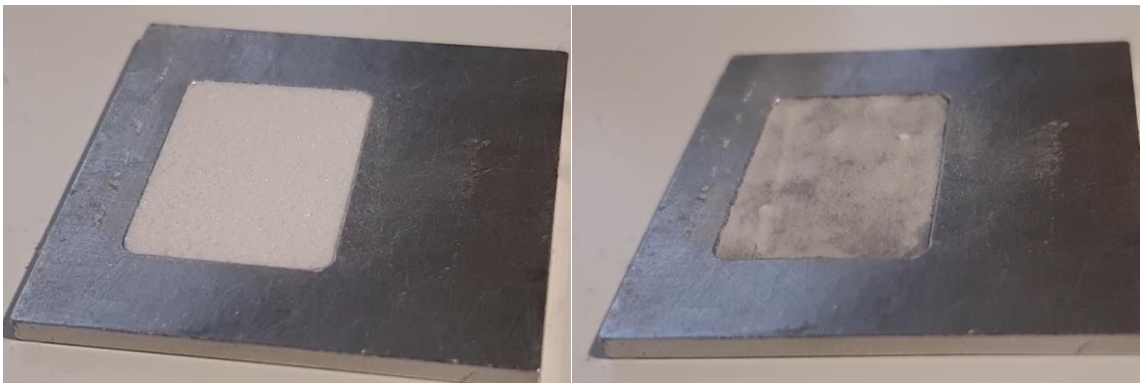

Figure 2.3. Morphology of the PM sample before (left) and after (right) heating to 423 K.

Table 2.1. Particle size measurement results.[48]

Sample	Particle Size /nm
COA300	300 ± 50
COA900	890 ± 170
CTC(SD)	1160 ± 220

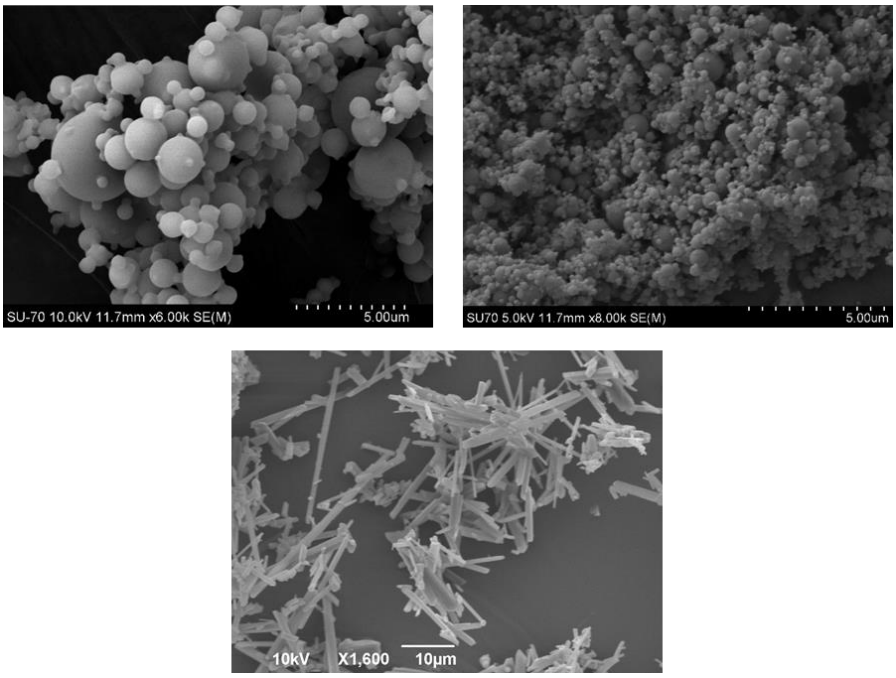

Figure 2.4. SEM images of COA900 (top left), COA300 (top right) and CTC(SD) (bottom).[48]

Thermal Analysis

TG and DSC

The results of the TG and DSC experiments on CEL, THC, CTC, COA900, COA300, CTC(SD) are illustrated in Figure 2.5. The values of the onset temperatures of the mass loss processes obtained by TG, and the fusion onset temperatures and fusion enthalpies obtained by DSC are summarized in Table 2.2. The uncertainties correspond to the standard error of 2 runs for TG results and 5 runs for DSC results.

The values obtained for the DSC fusion onset temperatures of CEL, THC and CTC are in good agreement with the results of the literature (437 K for CTC, 434 K for CEL and 454 K for THC).[46] The CTC(SD) sample showed very similar results to the CTC sample.

The DSC results of the CEL, THC, CTC, and CTC(SD) samples show no signals other than fusion. The nanosized coamorphous samples showed a broad exothermic signal before fusion, which was later assigned to the cold crystallization of the sample to produce cocrystal based on HSM observations. It is worth noting that the onset temperature of this peak was 15 K lower for the sample of smaller particle size. This may be associated with the higher instability of this sample due to the higher surface to bulk ratio of the particles.[53] The coamorphous samples revealed a considerable variability in different runs, as evidenced by the high uncertainty of the average T_{on} values.

The fusion enthalpy of the melting peak of the coamorphous samples was lower than the fusion enthalpy of the pure cocrystal. Moreover, the melting peak of the coamorphous samples resulted in a higher absolute enthalpy value than the first signal. This, however, must be evoked having in mind the high standard errors associated with these measurements. If this difference is factual, it can be evidence that the coamorphous samples produced trough spray drying already possess crystalline domains.

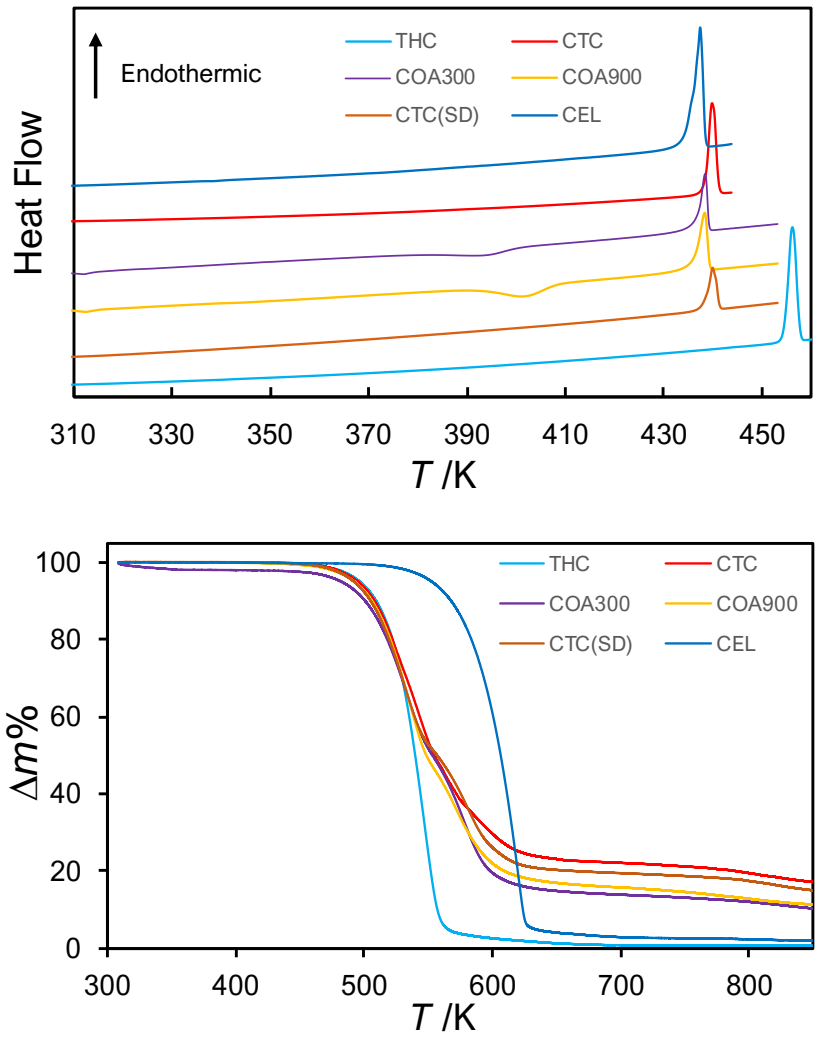

Figure 2.5. DSC curves (at 5 K·min^{-1}) for CEL, THC, CTC, COA900, COA300, CTC(SD) (top) and the corresponding TG curves at the same heating rate (bottom).

TG results show that the pure compounds, CEL and THC, have a monotonic behavior with two different temperature offsets, 577.6 K and 521.5 K, respectively. The binary samples showed a two-step thermal decomposition suggesting the decomposition of THC followed by the decomposition of CEL. The onset temperatures were slightly lower than for CEL. Until the second step of the thermal decomposition the curve profile is very similar for all binary samples, despite this, the second step shows higher variability with the final mass plateauing at different values following the order, COA300 < COA900 < CTC(SD) ≈ CTC. This series correlates well with the stability hierarchy obtained in this work (see section Stability of Cocrystals and Coamorphous materials).

Table 2.2. Values obtained for the onsets of the mass loss processes obtained by TG, fusion onset temperatures and fusion enthalpy both obtained by DSC.

Sample	T_{on} /K (mass loss)	T_{on} /K (fusion)	$\Delta_{fus}H_m$ /kJ·mol^{-1}
CEL	577.6 ± 10.1	435.06 ± 0.04	36.5 ± 0.1
THC	521.5 ± 12.8	453.5 ± 0.1	35.4 ± 0.1
CTC	512.9 ± 1.2	438.1 ± 0.1	62.5 ± 1.3
COA300 (1st signal)	497.3 ± 0.2	380.2 ± 8.5	-46.4 ± 6.0
COA300 (2nd signal)		437.0 ± 0.2	50.1 ± 0.5
COA900 (1st signal)	508.1 ± 7.1	394.0 ± 4.1	-49.9 ± 2.7
COA900 (2nd signal)		437.4 ± 0.6	51.5 ± 0.5
CTC(SD)	497.1 ± 3.1	438.6 ± 0.6	62.4 ± 0.8

HSM

The coamorphous sample with particle size of 900 nm was analyzed by HSM. The results, illustrated in Figure 2.6, complement the DSC observations and the observations from Figure 2.3. The initial heating to 418 K showed the amorphous sample liquifying from 363 K (Figure 2.6b) to 383 K (Figure 2.6c). Immediately after, the sample crystalized up to 393 K (Figure 2.6d and Figure 2.6e). The second heating cycle showed the crystallized sample melting in the temperature range of 427-444 K (Figure 2.6f) and after cooling the formation of small crystals (Figure 2.6g). Unlike the first crystallization, the second one did not occur for all the samples, and after reaching room temperature (298 K), some amorphous regions were still present.

Stability of Cocrystals and Coamorphous materials

To determine the thermodynamic stability of the produced crystalline and amorphous materials, a combination of calorimetric and solubility measurements was performed. As presented in the Introduction, the thermodynamic stability was evaluated based on the reaction:

$$\mathrm{THC{:}\,CEL(cr/am)} \rightarrow \mathrm{THC(cr)} + \mathrm{CEL(cr)} \tag{2.5}$$

The enthalpy of reaction (2.5), $\Delta_r H_m^\circ(2.5)$, was obtained from solution calorimetry measurements. The corresponding Gibbs energy, $\Delta_r G_m^\circ(2.5)$ was determined from solubility measurements. The entropic factor, $T\Delta_r S_m^\circ(2.5)$, was derived from both types of results using equation (2.2).

Solution calorimetry

To determine the enthalpic factor of Equation 2.2 enthalpies of solution of different materials were measured using solution calorimetry. The measured processes were the following:

$$\mathrm{THC{:}\,CEL(cr/am)} + n\mathrm{DMSO(l)} \rightarrow (\mathrm{THC} + \mathrm{CEL} + n\mathrm{DMSO})(\mathrm{sln}) \tag{2.6}$$

$$\mathrm{THC(cr)} + \mathrm{nDMSO(l)} \rightarrow (\mathrm{THC} + \mathrm{nDMSO})(\mathrm{sln}) \tag{2.7}$$

$$\mathrm{CEL(cr)} + (\mathrm{THC} + \mathrm{nDMSO})(\mathrm{sln}) \rightarrow (\mathrm{THC} + \mathrm{CEL} + \mathrm{nDMSO})(\mathrm{sln}) \tag{2.8}$$

where *n* is the amount of DMSO used in the experiments per mol of dissolved material.

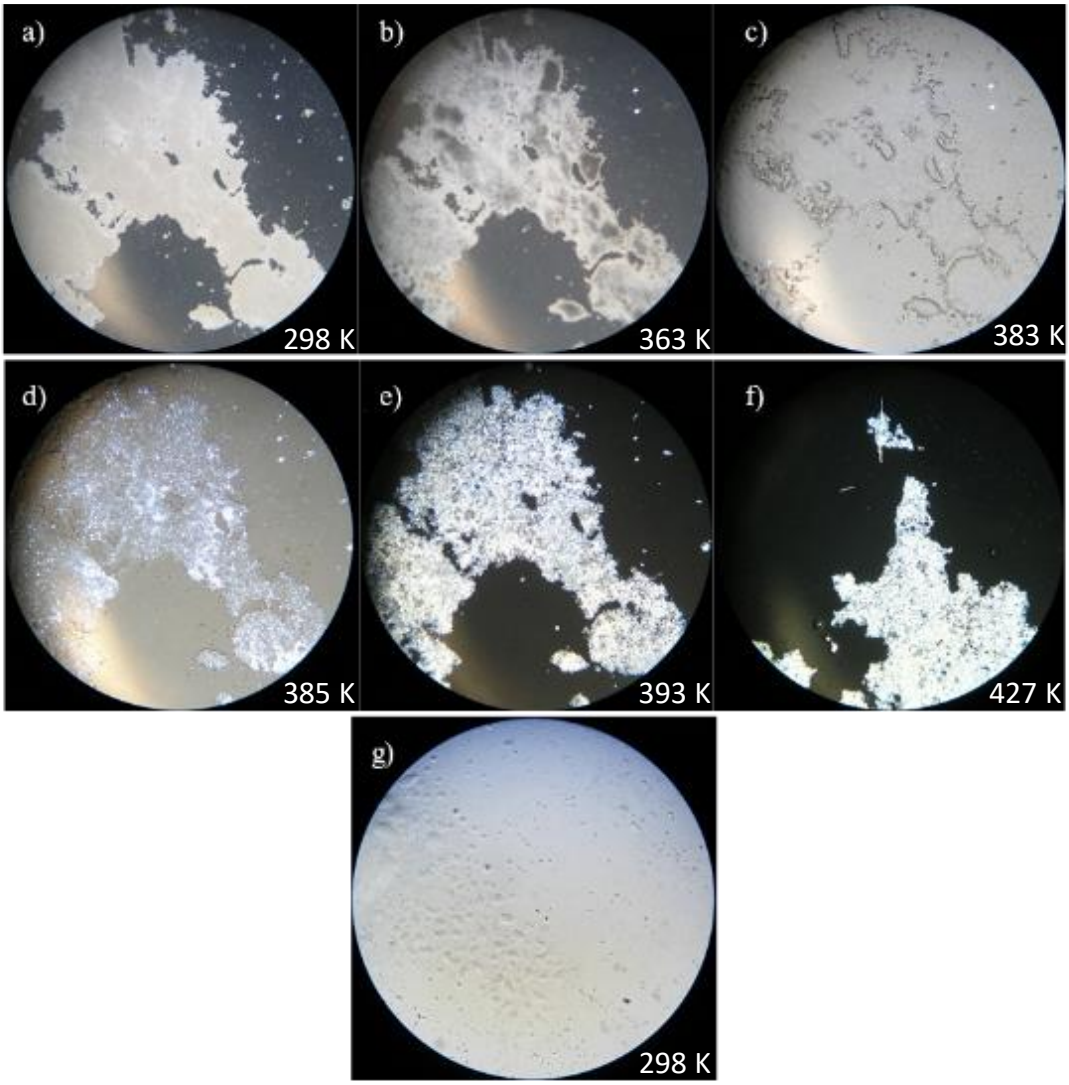

Figure 2.6. HSM images under 200× magnification, using crossed polarizers (except images c. and g), of the cold crystallization of COA900 sample and the subsequent fusion of the crystallized sample. The approximate temperature at which the images were taken are in the lower right corner.

Equations 2.6-2.8, lead to:

$$\Delta_{\mathrm{r}}H^{\circ}_{\mathrm{m}}(2.5) = \Delta_{\mathrm{sol}}H^{\circ}_{\mathrm{m}}(2.6) - \Delta_{\mathrm{sol}}H^{\circ}_{\mathrm{m}}(2.7) - \Delta_{\mathrm{sol}}H^{\circ}_{\mathrm{m}}(2.8) \qquad (2.9)$$

The obtained enthalpies of the processes in equations 2.6-2.8 (shown in Table S 1 to Table S 6) are summarized in Table 2.3 along with the corresponding enthalpies of reaction 2.5. The area contributed by the drop processed , A_b, is 15.913 ± 0.574 mV·s.

The $\Delta_{\mathrm{r}}H^{\circ}_{\mathrm{m}}(2.5)$ results show that:

(*i*) Only the cocrystal sample produced by crystallization from solution gave an endothermic decomposition reaction. This indicates that on enthalpic grounds the lattice enthalpy of CTC is larger than the combined values of its precursors and the opposite occurs for CTC(SD), COA300, and COA900. Thus, only the formation of the cocrystal trough solution crystallization leads to an enthalpic stability advantage relative to the precursors.

(*ii*) The enthalpy of reaction (2.5) decreases (becomes more negative) as the particle size decreases. This is the expected trend, since the increase of the surface to bulk ratio as the particle size decreases, leads to lower thermodynamic stability.[54]

Table 2.3. Enthalpies of solution and reaction at 298.15 K (data in kJ·mol^{-1}).

	CTC	CTC(SD)	COA300	COA900
$\Delta_{\mathrm{sol}}H^{\circ}_{\mathrm{m}}(2.7)$		7.08 ± 0.49		
$\Delta_{\mathrm{sol}}H^{\circ}_{\mathrm{m}}(2.8)$		0.78 ± 0.22		
$\Delta_{\mathrm{sol}}H^{\circ}_{\mathrm{m}}(2.6)$	12.75 ± 0.23	6.17 ± 0.36	-17.00 ± 0.83	-15.59 ± 0.63
$\Delta_{\mathrm{r}}H^{\circ}_{\mathrm{m}}(2.5)$	4.89 ± 0.58	-1.69 ± 0.48	-24.86 ± 0.89	-23.45 ± 0.71

Enthalpy of dissociation recuring to DSC

A common methodology to measure the dissociation enthalpy of cocrystals is the use of DSC to obtain a fusion enthalpy of a physical mixture of the cocrystal precursors PM and of the cocrystal itself.[55] This processes, includes the additional energy needed to cool and heat the components, and can be arranged in a thermodynamic cycle in order to determine the cocrystal dissociation enthalpy (Figure 2.7). In this work, this methodology was also applied to obtain the enthalpy of reaction 2.5 based on the equation.

$$\Delta_{\mathrm{r}}H^{\circ}_{\mathrm{m}}(2.5) = \Delta_{\mathrm{fus}}H_{\mathrm{m}}(\mathrm{A})[\text{process a}] - \Delta_{\mathrm{fus+mix}}H_{\mathrm{m}}(\mathrm{PM})[\text{process d}] \qquad (2.10)$$

This process assumes that the enthalpy associated with heating the cocrystal to the melting temperature (i.e. process a in Figure 2.7) is equal to the energy released when the components are cooled (i.e. processes c and e in Figure 2.7):

$$\int_{T}^{T_{\mathrm{m,A}}} C^{\mathrm{s}}_{\mathrm{p,A}}dT\,[\text{process a}] = \int_{T_{\mathrm{m,A}}}^{T_{\mathrm{m,CEL+THC}}} C^{\mathrm{l}}_{\mathrm{p,A}}dT\,[\text{process c}] + \int_{T_{\mathrm{m,CEL+THC}}}^{T} \left(C^{\mathrm{s}}_{\mathrm{p,CEL}} + C^{\mathrm{s}}_{\mathrm{p,THC}}\right)dT\,[\text{process e}] \qquad (2.11)$$

where *A* corresponds to the cocrystal/coamorph, $T_{\mathrm{m,A}}$ and $T_{\mathrm{m,CEL+THC}}$ the melting temperatures of A and the physical mixture, respectively, $C^{s}_{\mathrm{p,A}}$, $C^{s}_{\mathrm{p,CEL}}$ and $C^{s}_{\mathrm{p,THC}}$, are the standard molar heat capacities the cocrystal/coamorph, CEL and THC, respectively, and $C^{l}_{p,A}$ the heat capacity of the cocrystal/coamorph material in the liquid state.

The obtained fusion enthalpies are summarized in Table 2.4 along with the corresponding enthalpies of reaction 2.5.

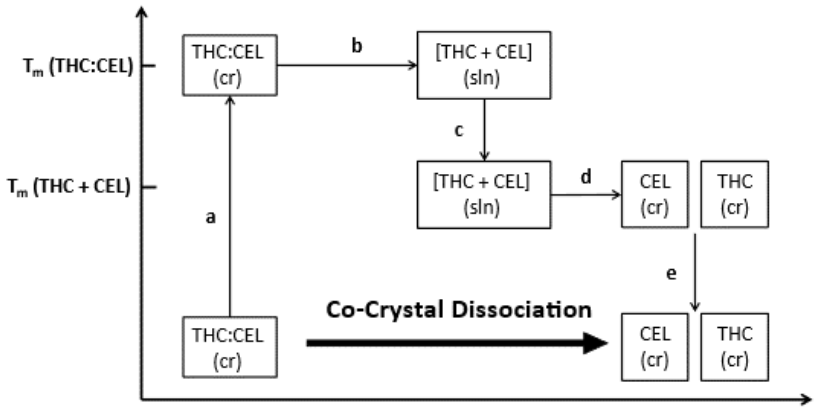

$$\mathrm{THC{:}\,CEL(cr/am, 298\ K)} \rightarrow \mathrm{THC{:}\,CEL}\left(\mathrm{cr/am}, \mathrm{T}_{m,(CTC)}\right) \quad \text{(a)}$$

$$\mathrm{THC{:}\,CEL}\left(\mathrm{cr/am}, \mathrm{T}_{m,(CTC)}\right) \rightarrow [\mathrm{THC + CEL}]\left(sln, \mathrm{T}_{m,(CTC)}\right) \quad \text{(b)}$$

$$[\mathrm{THC + CEL}]\left(sln, \mathrm{T}_{m,(CTC)}\right) \rightarrow [\mathrm{THC + CEL}]\left(sln, \mathrm{T}_{m,(CEL+THC)}\right) \quad \text{(c)}$$

$$[\mathrm{THC + CEL}]\left(sln, \mathrm{T}_{m,(CEL+THC)}\right) \rightarrow \mathrm{THC}\left(cr, \mathrm{T}_{m,(CEL+THC)}\right) + \mathrm{CEL}\left(cr, \mathrm{T}_{m,(CEL+THC)}\right) \quad \text{(d)}$$

$$\mathrm{THC}\left(cr, \mathrm{T}_{m,(CEL+THC)}\right) + \mathrm{CEL}\left(cr, \mathrm{T}_{m,(CEL+THC)}\right) \rightarrow \mathrm{THC}(cr, 298\ \mathrm{K}) + \mathrm{CEL}(cr, 298\ \mathrm{K}) \quad \text{(e)}$$

$$\mathrm{THC{:}\,CEL(cr/am, 298\ K)} \rightarrow \mathrm{THC}(cr, 298\ \mathrm{K}) + \mathrm{CEL}(cr, 298\ \mathrm{K})$$

Figure 2.7. Thermodynamic cycle for cocrystal dissociation and respective processes in the cycle

Table 2.4. Enthalpies of fusion and reaction at 298.15 K (data in kJ·mol^{-1})

	CTC	CTC(SD)	COA300	COA900
$\Delta_{\mathrm{fus+mix}}H_{\mathrm{m}}(\mathrm{PM})$		38.9 ± 3.6		
$\Delta_{\mathrm{fus}}H_{\mathrm{m}}(\mathrm{A})$	62.5 ± 1.3	62.4 ± 0.8	3.8 ± 6	1.6 ± 2.7
$\Delta_{\mathrm{r}}H_{\mathrm{m}}^{\circ}(2.5)$	23.5 ± 3.8	23.5 ± 3.7	-35.2 ± 7	-37.4 ± 4.5

Comparing the values obtained through solution calorimetry and DSC major differences can be noted:

(i) The DSC results showed identical results, $\Delta_{\mathrm{r}}H_{\mathrm{m}}(2.5)$, for the two crystalline samples and gave a higher stability, on enthalpic grounds, than the results from solution calorimetry. In fact, the instability, $\Delta_{\mathrm{r}}H_{\mathrm{m}}(2.5) < 0$, noted for CTC(SD) by solution calorimetry was not detected by DSC.

(ii) In contrast, for the coamorphous samples, if the combined uncertainty intervals are disregarded, the $\Delta_{\mathrm{r}}H_{\mathrm{m}}(2.5)$ vs. particle size trend observed through solution calorimetry was captured with the reverse behavior, albeit being significantly more negative $\Delta_{\mathrm{r}}H_{\mathrm{m}}(2.5)$. Here, the smaller particles showed a higher enthalpy value, meaning that they are more stable. This fact, however, must be weighed up with the large error associated with these values, which translates into an inability to establish a particle size/stability relationship from the DSC results.

(iii) Data obtained by the two methods only confirms the fact that the coamorphous samples present a higher instability ($\Delta_{\mathrm{r}}H_{\mathrm{m}}(2.5) \ll 0$) than crystalline materials.

(iv) Finally, the DSC experiments seem to overestimate the $\Delta_r H_m(2.5)$ obtained through solution calorimetry.

The difference between the solution calorimetry and the DSC results must be systematically addressed. In this work a preliminary study is made to compare both methods. Nonetheless, several approximations were made for the DSC methodology.

Solubility measurements

The knowledge of a compound equilibrium solubility can be correlated with the Gibbs energy of the dissolution process:[43]

$$\Delta_{\text{diss}} G_{\text{m}}^{\circ} = -RT \ln K_{\text{sp}} \tag{2.12}$$

Using this concept, we determined the Gibbs energies of the following processes at 298.15 ± 0.10 K through solubility studies:

$$\text{CEL(cr)} \rightleftharpoons \text{CEL(sln)} \tag{2.13}$$

$$\text{THC(cr)} \rightleftharpoons \text{THC(sln)} \tag{2.14}$$

$$\text{CTC(cr)} \rightleftharpoons \text{CEL(sln)} + \text{THC(sln)} \tag{2.15}$$

$$\text{CTC(SD)(cr)} \rightleftharpoons \text{CEL(sln)} + \text{THC(sln)} \tag{2.16}$$

$$\text{COA300(am)} \rightleftharpoons \text{CEL(sln)} + \text{THC(sln)} \tag{2.17}$$

$$\text{COA900(am)} \rightleftharpoons \text{CEL(sln)} + \text{THC(sln)} \tag{2.18}$$

$$\text{CEL(cr)} + \text{THC(cr)} \rightleftharpoons \text{CEL(sln)} + \text{THC(sln)} \tag{2.19}$$

The equilibrium solubilities are presented in Table 2.5. It should be noted that aside from equilibrium solubilities, a preliminary dissolution kinetic study was conducted for COA900 to confirm that the coamorphous sample did not decompose into the precursors or crystallized in contact with the solution. This test gauged if solubility values could be traced to the amorphous solid and be included the thermodynamic analysis. The results are illustrated in Figure 2.8.

Furthermore, the stoichiometric coefficient, which accounts for the incongruent dissolution of the two compounds, was obtained as:

$$a = \frac{n_{\text{CEL}} - n_{THC}}{n_{\text{CEL}}} \tag{2.20}$$

where n_{CEL} and n_{THC} are the amounts of substance of CEL and THC, respectively, present in solution. This value increases if dissolution is less congruent, it is equal to 0 for a congruent dissolution.

The Gibbs energy of reaction 2.5 was obtained from:

$$\Delta_r G_{\text{m}}^{\circ}(2.5) = -RT \ln \left[\left(\frac{x_{\text{CEL}}}{x'_{\text{CEL}}} \right) \left(\frac{x_{\text{THC}}}{x'_{\text{THC}}} \right)^{1-a} \right] \tag{2.21}$$

Based on the solubility measurements corresponding to equations 2.13 to 2.19. In equation (2.21), whose derivation can be found elsewhere,[56] x_{CEL} and x_{THC} represent the mole fractions of CEL and THC, respectively, in equilibrium with the cocrystal, and x'_{CEL} and x'_{THC} represent the mole fractions of CEL and THC, respectively. The preliminary dissolution rate measurements (Figure 2.8) show that the dissolution of the COA900 sample increases very rapidly but immediately after the first measurement (t = 30 s) the solution concentration starts dropping. This indicates that the coamorphous samples are not stable in contact with the solution and immediately start crystallizing. We cannot, therefore, use the solubility values for these samples to extract $\Delta_r G_m^o(2.5)$ from solubility measurements.

Table 2.5. Solubility and Gibbs free energy results. Uncertainties correspond to twice the standard error of 3 runs.

	CTC	CTC(SD)	COA300	COA900	PM
x_{CEL} ($\times 10^3$)	0.95 ± 0.03	0.86 ± 0.02	1.07 ± 0.03	0.98 ± 0.01	0.91 ± 0.03
x_{THC} ($\times 10^3$)	0.79 ± 0.02	0.79 ± 0.02	0.76 ± 0.06	0.66 ± 0.02	0.69 ± 0.05
x'_{CEL} ($\times 10^3$)			2.78 ± 0.02		
x'_{THC} ($\times 10^3$)			2.95 ± 0.11		
a	0.17 ± 0.03	0.08 ± 0.05	0.29 ± 0.06	0.33 ± 0.02	0.24 ± 0.06
$\Delta_r G_m^\circ$ /kJ·mol^{-1}	5.4 ± 1.5	5.9 ± 2.4	-	-	-

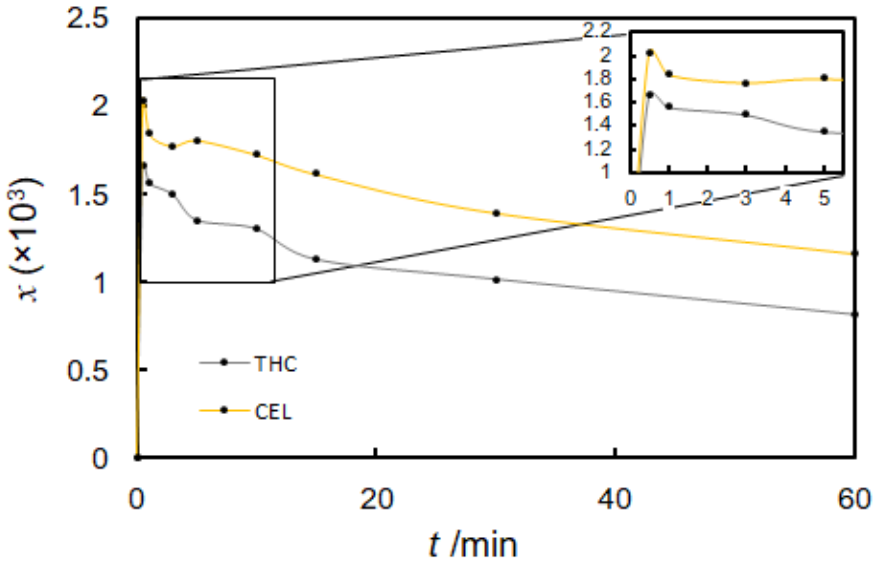

Figure 2.8. Preliminary dissolution profile for the COA900 sample.

The solubilities of all samples that included both components are much lower than those of the pure components. In addition, all these samples showed similar values, which were all very close to the CTC solubility. This can be an indication that in contact with the solvent all samples start crystallizing. Because of this, Gibbs free energy was only calculated for the crystalline samples, i.e. CTC and CTC(SD), which gave similar results within the experimental error. None of the samples presented a congruent dissolution, with CTC(SD) (a = 0.08 ± 0.05) being the closest and COA900 sample (a = 0.33 ± 0.02) furthest from congruent dissolution. The a value for the latter was very close to the that obtained for the COA300 coamorphous sample (a = 0.29 ± 0.06).

Energetics overview

The thermodynamic results obtained from solution calorimetry and solubility measurements lead to $T\Delta_r S°_m(2.5)$ = -0.51 ± 1.57 kJ·mol^{-1} for CTC and $T\Delta_r S°_m(2.5)$ = -7.6 ± 2.4 kJ·mol^{-1} for CTC(SD). If, instead of the enthalpy of reaction results from solution calorimetry, we use the values obtained with the DSC methodology, this trend would not be seen, and the entropic contribution would be positive for both samples.

Figure 2.9 summarizes the obtained thermodynamic results which show that the dissociation reaction of both crystalline samples is endergonic ($\Delta_r G°_m > 0$, at 298.15 K). It indicates that they are thermodynamically stable relative to the decomposition into the individual precursors. Nonetheless, the two crystalline samples exhibit different types of stabilization. More specifically the stabilization of the CTC sample is of enthalpic nature ($\Delta_r H°_m > |T\Delta_r S°_m|$) while that of CTC(SD) is of entropic nature ($\Delta_r H°_m < |T\Delta_r S°_m|$). These results can be rationalized based on the surface to bulk ratio associated with the different particle sizes, as the particle gets smaller the surface to bulk ratio increases. Since the surface of a particle is more unstable than the bulk the smaller particles present lower internal energy. Moreover, smaller particle sizes exhibit higher disorder, resulting in an higher entropy state.

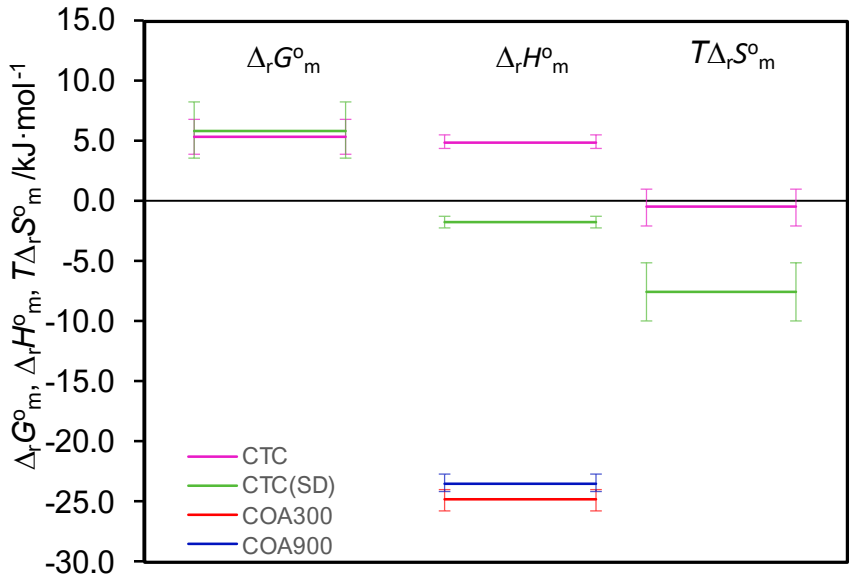

Figure 2.9. Comparison of the Gibbs energies, enthalpies, and entropies of reaction 2.5.

2.4 Conclusion

The synthesis of Tramadol hydrochloride:Celecoxib cocrystal was successfully performed using ball milling, crystallization from solution, and crystallization from melt. Thermal analysis of these crystalline samples, the precursors, and coamorphous and cocrystalline nanoparticles produced in Ireland by spray drying as previously described,[48] was performed using TG, DSC and HSM. TG results showed similar behaviors for all bicomponent samples that revealed a behavior in-between those of the two precursors. DSC results agree with literature for the previously described materials. All crystalline samples show only one signal, and the coamorphous samples show a broad signal before fusion, at ~390 K, which was confirmed to be cold crystallization of the cocrystal that subsequently melts.

The thermodynamic stability of these materials was studied relative to the decomposition into the precursors. The enthalpic factor of the Gibbs energy was determined using both solution calorimetry and DSC measurements. Solution calorimetry revealed that, on enthalpic grounds, the cocrystal produced trough solution crystallization was stable, the cocrystal produced trough spray drying was marginally unstable, and the coamorphous nanoparticles were more unstable, with the smaller nanoparticles showing a slightly higher instability than the larger size nanoparticles. The same measurement made through DSC showed that, on enthalpic grounds, the two cocrystalline samples are equally stable and the coamorphous nanoparticles are even more unstable than observed by solution calorimetry. Furthermore, the relative stability of the latter (smaller particles more stable) is not coherent and opposite to that given by solution calorimetry. The enthalpy values obtained by DSC are also considerably higher than those obtained by solution calorimetry. Thus, overall DSC does not seem to be an adequate method to study the energetics of formation of Tramadol hydrochloride:Celecoxib materials. The analysis of the overall energetics determined in this work by solution calorimetry shows that: (i) both crystalline samples are stable relative to decomposition into their precursors ($\Delta_r G°_m(2.5) > 0$); (ii) the stability of the cocrystalline sample produced through solution crystallization is of enthalpic nature ($\Delta_r H°_m > |T\Delta_r S°_m|$) while that of the cocrystalline sample produced through spray drying is of entropic nature ($\Delta_r H°_m < |T\Delta_r S°_m|$).

Bibliography

(1) Dahl, T.; Hassel, O.; Ballhausen, C. J.; Ragnarsson, U.; Rasmussen, S. E.; Sunde, E.; Sørensen, N. A. Solid Adducts of Hexamethylenetetramine and Trihalogenomethanes. Crystal Structure of the 1:1 Iodoform Compound. *Acta Chem. Scand.* **1970**, *24*, 377–383.

(2) Hassel, O.; Hvoslef, J.; Vihovde, E. H.; Sörensen, N. A. The Structure of Bromine 1,4-Dioxanate. *Acta Chem. Scand.* **1954**, *8*, 873–873.

(3) Bent, H. A. Structural Chemistry of Donor-Acceptor Interactions. *Chem. Rev.* **1968**, *68* (5), 587–648.

(4) Brinck, T.; Murray, J. S.; Politzer, P. Surface Electrostatic Potentials of Halogenated Methanes as Indicators of Directional Intermolecular Interactions. *Int. J. Quantum Chem.* **1992**, *44* (S19), 57–64.

(5) Costa, P. J. The Halogen Bond: Nature and Applications. *Phys. Sci. Rev. 2* (11).

(6) Cavallo, G.; Metrangolo, P.; Milani, R.; Pilati, T.; Priimagi, A.; Resnati, G.; Terraneo, G. The Halogen Bond. *Chem. Rev.* **2016**, *116* (4), 2478–2601.

(7) Metrangolo, P.; Murray, J. S.; Pilati, T.; Politzer, P.; Resnati, G.; Terraneo, G. Fluorine-Centered Halogen Bonding: A Factor in Recognition Phenomena and Reactivity. *Cryst. Growth Des.* **2011**, *11* (9), 4238–4246.

(8) Desiraju, G. R.; Parthasarathy, R. The Nature of Halogen-Halogen Interactions: Are Short Halogen Contacts Due to Specific Attractive Forces or Due to Close Packing of Nonspherical Atoms? *J. Am. Chem. Soc.* **1989**, *111* (23), 8725–8726.

(9) Aakeröy, C. B.; Spartz, C. L.; Dembowski, S.; Dwyre, S.; Desper, J. A Systematic Structural Study of Halogen Bonding versus Hydrogen Bonding within Competitive Supramolecular Systems. *IUCrJ* **2015**, *2*, 498–510.

(10) Nayak, A.; Pedireddi, V. R. A Study of Hierarchy of Hydrogen and Halogen Bonds in the Molecular Complexes of 4-Iodophenol with Various Aza-Donor Compounds. *J. Mol. Struct.* **2017**, *1130*, 251–263.

(11) Takemura, A.; McAllister, L. J.; Karadakov, P. B.; Pridmore, N. E.; Whitwood, A. C.; Bruce, D. W. Competition and Cooperation: Hydrogen and Halogen Bonding in Co-Crystals Involving 4-Iodotetrafluorobenzoic Acid, 4-Iodotetrafluorophenol and 4-Bromotetrafluorophenol. *CrystEngComm* **2014**, *16* (20), 4254–4264.

(12) Laurence, C.; Graton, J.; Berthelot, M.; El Ghomari, M. J. The Diiodine Basicity Scale: Toward a General Halogen-Bond Basicity Scale. *Chem. – A Eur. J.* **2011**, *17* (37), 10431–10444.

(13) Takemura, A.; McAllister, L. J.; Hart, S.; Pridmore, N. E.; Karadakov, P. B.; Whitwood, A. C.; Bruce, D. W. Halogen- and Hydrogen-Bonded Salts and Co-Crystals Formed from 4-Halo-2,3,5,6-Tetrafluorophenol and Cyclic Secondary and Tertiary Amines: Orthogonal and Non-Orthogonal Halogen and Hydrogen Bonding, and Synthetic Analogues of Halogen-Bonded Biological Systems. *Chem. – A Eur. J.* **2014**, *20* (22), 6721–6732.

(14) Aakeröy, C. B.; Baldrighi, M.; Desper, J.; Metrangolo, P.; Resnati, G. Supramolecular Hierarchy among Halogen-Bond Donors. *Chem. - A Eur. J.* **2013**, *19* (48), 16240–16247.

(15) Aakeröy, C. B.; Fasulo, M.; Schultheiss, N.; Desper, J.; Moore, C. Structural Competition between Hydrogen Bonds and Halogen Bonds. *J. Am. Chem. Soc.* **2007**, *129* (45), 13772–13773.

(16) Aakeroy, C. B.; Chopade, P. D.; Ganser, C.; Desper, J. Facile Synthesis and Supramolecular Chemistry of Hydrogen Bond/Halogen Bond-Driven Multi-Tasking Tectons. *Chem.*

Commun. **2011**, *47* (16), 4688–4690.

(17) Tothadi, S.; Desiraju, G. R. Designing Ternary Cocrystals with Hydrogen Bonds and Halogen Bonds. *Chem. Commun.* **2013**, *49* (71), 7791–7793.

(18) Aakeröy, C. B.; Forbes, S.; Desper, J. Using Cocrystals To Systematically Modulate Aqueous Solubility and Melting Behavior of an Anticancer Drug. *J. Am. Chem. Soc.* **2009**, *131* (47), 17048–17049.

(19) Scheiner, S. Enhancement of Halogen Bond Strength by Intramolecular H-Bonds. *J. Phys. Chem. A* **2023**, *127* (21), 4695–4703.

(20) Macrae, C. F.; Sovago, I.; Cottrell, S. J.; Galek, P. T. A.; McCabe, P.; Pidcock, E.; Platings, M.; Shields, G. P.; Stevens, J. S.; Towler, M.; Wood, P. A. Mercury 4.0 : From Visualization to Analysis, Design and Prediction. *J. Appl. Crystallogr.* **2020**, *53* (1), 226–235.

(21) APEX2. Bruker Analytical Systems: Madison 2005.

(22) Sheldrick, G. M.; IUCr. A Short History of SHELX. *urn:issn:0108-7673* **2007**, *64* (1), 112–122.

(23) Sheldrick, G. M.; IUCr. Crystal Structure Refinement with SHELXL. *urn:issn:2053-2296* **2015**, *71* (1), 3–8.

(24) Farrugia, L. J. WinGX Suite for Small-Molecule Single-Crystal Crystallography. *J. Appl. Crystallogr.* **1999**, *32* (4), 837–838.

(25) Zhao, Y.; Truhlar, D. G. The M06 Suite of Density Functionals for Main Group Thermochemistry, Thermochemical Kinetics, Noncovalent Interactions, Excited States, and Transition Elements: Two New Functionals and Systematic Testing of Four M06-Class Functionals and 12 Other Functionals. *Theor. Chem. Acc.* **2008**, *120* (1–3), 215–241.

(26) Kendall, R. A.; Dunning, T. H.; Harrison, R. J. Electron Affinities of the First-row Atoms Revisited. Systematic Basis Sets and Wave Functions. *J. Chem. Phys.* **1992**, *96* (9), 6796–6806.

(27) M. J. Frisch, G. W. Trucks, H. B. Schlegel, G. E. Scuseria, M. A. Robb, J. R. Cheeseman, G. Scalmani, V. Barone, B. Mennucci, G. A. Petersson, H. Nakatsuji, M. Caricato, X. Li, H. P. Hratchian, A. F. Izmaylov, J. Bloino, G. Zheng, J. L. Sonnenberg, M. Had, and D. J. F.; Frisch, M. J.; Trucks, G. W.; Schlegel, H. B.; Scuseria, G. E.; Robb, M. A.; Cheeseman, J. R.; Scalmani, G.; Barone, V.; Mennucci, B.; Petersson, G. A.; Nakatsuji, H.; Caricato, M.; Li, X.; Hratchian, H. P.; Izmaylov, A. F.; Bloino, J.; Zheng, G.; Sonnenberg, J. L.; Hada, M.; Ehara, M.; Toyota, K.; Fukuda, R.; Hasegawa, J.; Ishida, M.; Nakajima, T.; Honda, Y.; Kitao, O.; Nakai, H.; Vreven, T.; Montgomery Jr., J. A.; Peralta, J. E.; Ogliaro, F.; Bearpark, M.; Heyd, J. J.; Brothers, E.; Kudin, K. N.; Staroverov, V. N.; Kobayashi, R.; Normand, J.; Raghavachari, K.; Rendell, A.; Burant, J. C.; Iyengar, S. S.; Tomasi, J.; Cossi, M.; Rega, N.; Millam, J. M.; Klene, M.; Knox, J. E.; Cross, J. B.; Bakken, V.; Adamo, C.; Jaramillo, J.; Gomperts, R.; Stratmann, R. E.; Yazyev, O.; Austin, A. J.; Cammi, R.; Pomelli, C.; Ochterski, J. W.; Martin, R. L.; Morokuma, K.; Zakrzewski, V. G.; Voth, G. A.; Salvador, P.; Dannenberg, J. J.; Dapprich, S.; Daniels, A. D.; Farkas, Ö.; Foresman, J. B.; Ortiz, J. V; Cioslowski, J.; Fox, D. J. Gaussian 09, Revision D.01. *Gaussian Inc., Wallingford*. 2013, p Wallingford CT.

(28) Boys, S. F.; Bernardi, F. The Calculation of Small Molecular Interactions by the Differences of Separate Total Energies. Some Procedures with Reduced Errors. *Mol. Phys.* **1970**, *19* (4), 553–566.

(29) Latajka, aw; Scheiner, S.; Chem Phys, J.; Latajka, Z.; Scheinert, S. Primary and Secondary Basis Set Superposition Error at the SCF and MP2 Levels. H3N--Li+ and H2O--Li+. *J. Chem. Phys.* **1987**, *87* (2), 1194–1204.

(30) Lampronti, G. I.; Michalchuk, A. A. L.; Mazzeo, P. P.; Belenguer, A. M.; Sanders, J. K. M.;

Bacchi, A.; Emmerling, F. Changing the Game of Time Resolved X-Ray Diffraction on the Mechanochemistry Playground by Downsizing. *Nat. Commun. 2021 121* **2021**, *12* (1), 1–9.

(31) Paris, O.; Li, C.; Siegel, S.; Weseloh, G.; Emmerling, F.; Riesemeier, H.; Erko, A.; Fratzl, P. A New Experimental Station for Simultaneous X-Ray Microbeam Scanning for Small- and Wide-Angle Scattering and Fluorescence at BESSY II. *urn:issn:0021-8898* **2006**, *40* (s1), s466–s470.

(32) Kaupp, G. Solid-State Molecular Syntheses: Complete Reactions without Auxiliaries Based on the New Solid-State Mechanism. *CrystEngComm* **2003**, *5* (23), 117–133.

(33) Benecke, G.; Wagermaier, W.; Li, C.; Schwartzkopf, M.; Flucke, G.; Hoerth, R.; Zizak, I.; Burghammer, M.; Metwalli, E.; Müller-Buschbaum, P.; Trebbin, M.; Förster, S.; Paris, O.; Roth, S. V.; Fratzl, P. A Customizable Software for Fast Reduction and Analysis of Large X-Ray Scattering Data Sets: Applications of the New DPDAK Package to Small-Angle X-Ray Scattering and Grazing-Incidence Small-Angle X-Ray Scattering. *urn:issn:1600-5767* **2014**, *47* (5), 1797–1803.

(34) Dabros, M.; Emery, P. R.; Thalladi, V. R.; Dabros, M.; Emery, P. R.; Thalladi, V. R. A Supramolecular Approach to Organic Alloys: Cocrystals and Three- and Four-Component Solid Solutions of 1,4-Diazabicyclo[2.2.2]Octane and 4-X-Phenols (X = Cl, CH3, Br). *Angew. Chemie - Int. Ed.* **2007**, *46* (22), 4132–4135.

(35) Alvarez, S. A Cartography of the van Der Waals Territories. *Dalt. Trans.* **2013**, *42* (24), 8617–8636.

(36) Blagden, N.; de Matas, M.; Gavan, P. T.; York, P. Crystal Engineering of Active Pharmaceutical Ingredients to Improve Solubility and Dissolution Rates. *Adv. Drug Deliv. Rev.* **2007**, *59* (7), 617–630.

(37) Rodriguez-Aller, M.; Guillarme, D.; Veuthey, J. L.; Gurny, R. Strategies for Formulating and Delivering Poorly Water-Soluble Drugs. *J. Drug Deliv. Sci. Technol.* **2015**, *30*, 342–351.

(38) Reintjes, T. *Solubility Enhancement with BASF Pharma Polymers Solubilizer Compendium*; BASF: Ludwigshafen, 2011.

(39) Qiao, N.; Li, M.; Schlindwein, W.; Malek, N.; Davies, A.; Trappitt, G. Pharmaceutical Cocrystals: An Overview. *Int. J. Pharm.* **2011**, *419* (1–2), 1–11.

(40) Putra, O. D.; Umeda, D.; Fujita, E.; Haraguchi, T.; Uchida, T.; Yonemochi, E.; Uekusa, H. Solubility Improvement of Benexate through Salt Formation Using Artificial Sweetener. *Pharm. 2018, Vol. 10, Page 64* **2018**, *10* (2), 64.

(41) Amani, M.; Saadati Ardestani, N.; Majd, N. Y. Utilization of Supercritical CO2 Gas Antisolvent (GAS) for Production of Capecitabine Nanoparticles as Anti-Cancer Drug: Analysis and Optimization of the Process Conditions. *J. CO2 Util.* **2021**, *46*, 101465.

(42) Kim, D. H.; Kim, Y. W.; Tin, Y. Y.; Soe, M. T. P.; Ko, B. H.; Park, S. J.; Lee, J. W. Recent Technologies for Amorphization of Poorly Water-Soluble Drugs. *Pharm. 2021, Vol. 13, Page 1318* **2021**, *13* (8), 1318.

(43) Atkins, P.; Paula, J. de; Keeler, J. *Physical Chemistry*, 12th ed.; Oxford University Press: Oxford, 2022.

(44) Perlovich, G. L. Formation Thermodynamics of Two-Component Molecular Crystals: Polymorphism, Stoichiometry, and Impact of Enantiomers. *Cryst. Growth Des.* **2020**, *20* (8), 5526–5537.

(45) Taylor, C. R.; Day, G. M. Evaluating the Energetic Driving Force for Cocrystal Formation. *Cryst. Growth Des.* **2018**, *18* (2), 892–904.

(46) Almansa, C.; Mercè, R.; Tesson, N.; Farran, J.; Tomàs, J.; Plata-Salamán, C. R. Co-Crystal

of Tramadol Hydrochloride-Celecoxib (Ctc): A Novel API-API Co-Crystal for the Treatment of Pain. *Cryst. Growth Des.* **2017**, *17* (4), 1884–1892.

(47) Cebrecos, J.; Carlson, J. D.; Encina, G.; Lahjou, M.; Sans, A.; Sust, M.; Vaqué, A.; Morte, A.; Gascón, N.; Plata-Salamán, C. Celecoxib-Tramadol Co-Crystal: A Randomized 4-Way Crossover Comparative Bioavailability Study. *Clin. Ther.* **2021**, *43* (6), 1051–1065.

(48) O'Sullivan, A.; Ryan, K. M.; Padrela, L. Amorphization versus Cocrystallization of Celecoxib-Tramadol Hydrochloride Using CO2-Assisted Nano-Spray Drying. *J. CO2 Util.* **2023**, *73*, 102529.

(49) Meija, J.; Coplen, T. B.; Berglund, M.; Brand, W. A.; De Bièvre, P.; Gröning, M.; Holden, N. E.; Irrgeher, J.; Loss, R. D.; Walczyk, T.; Prohaska, T. Atomic Weights of the Elements 2013 (IUPAC Technical Report). *Pure Appl. Chem.* **2016**, *88* (3), 265–291.

(50) Feliciano, I. O.; Silva, D. P.; Piedade, M. F. M.; Bernardes, C. E. S.; Minas da Piedade, M. E. First and Second Dissociation Enthalpies in Bi-Component Crystals Consisting of Maleic Acid and L-Phenylalanine. *Mol. 2021, Vol. 26, Page 5714* **2021**, *26* (18), 5714.

(51) Bernardes, C. E. S.; Feliciano, I. O.; Naese, C.; Emmerling, F.; da Piedade, M. E. M. Energetics of Dehydroepiandrosterone Polymorphs I and II from Solution and Drop-Sublimation Calvet Microcalorimetry Measurements. *J. Chem. Thermodyn.* **2023**, *186*, 107137.

(52) Bento, R. N.; Rendas, M. A.; Semedo, V. A. R.; Bernardes, C. E. S.; Santos, M. S. C. S.; Diogo, H. P.; Antunes, F.; Minas da Piedade, M. E. The Standard Molar Enthalpy of the Base Catalysed Hydrolysis of Methyl Paraben Revisited. *J. Chem. Thermodyn.* **2016**, *103*, 176–180.

(53) Nanda, K. K. Size-Dependent Melting of Nanoparticles: Hundred Years of Thermodynamic Model. *Pramana* **2009**, *72* (4), 617–628.

(54) Range, S.; Bernardes, C. E. S.; Simões, R. G.; Epple, M.; da Piedade, M. E. M. Size Matters: An Experimental and Computational Study of the Influence of Particle Size on the Lattice Energy of NaCl. *J. Phys. Chem. C* **2015**, *119* (8), 4387–4396.

(55) Svärd, M.; Ahuja, D.; Rasmuson, Å. C. Calorimetric Determination of Cocrystal Thermodynamic Stability: Sulfamethazine-Salicylic Acid Case Study. *Cryst. Growth Des.* **2020**, *20* (7), 4243–4251.

(56) Évora, A. O. L.; Bernardes, C. E. S.; Piedade, M. F. M.; Conceição, A. C. L.; Minas Da Piedade, M. E. Energetics of Glycine Cocrystal or Salt Formation with Two Regioisomers: Fumaric Acid and Maleic Acid. *Cryst. Growth Des.* **2019**, *19* (9), 5054–5064.

Supplementary Information

Figures S1-S39: Comparison of the PXRD of the products and precursors involved in the cocrystal screening

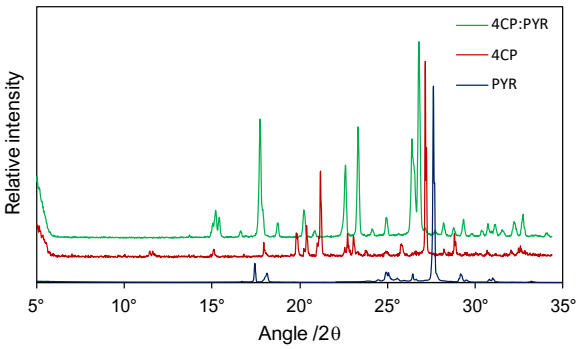

Figure S 1. 4CP$_2$:PYR

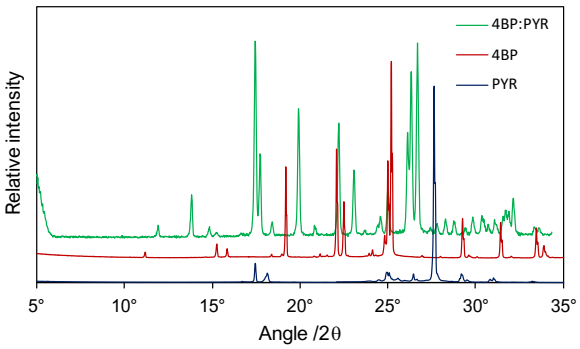

Figure S 2. 4BP$_2$:PYR

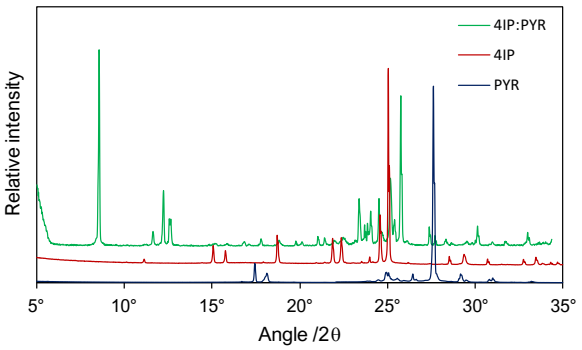

Figure S 3. 4IP$_2$:PYR

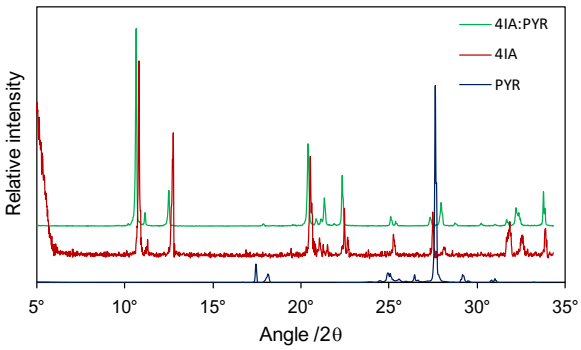

Figure S 4. 4IA$_2$:PYR

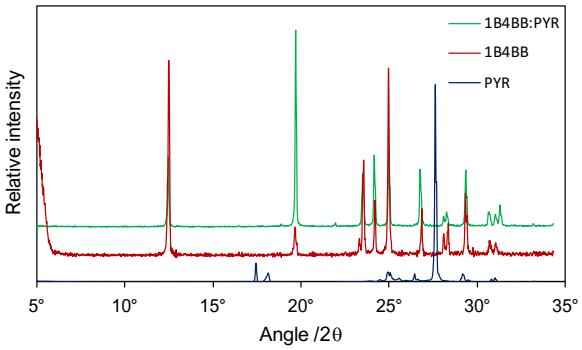

Figure S 5. 1B4BB$_2$:PYR

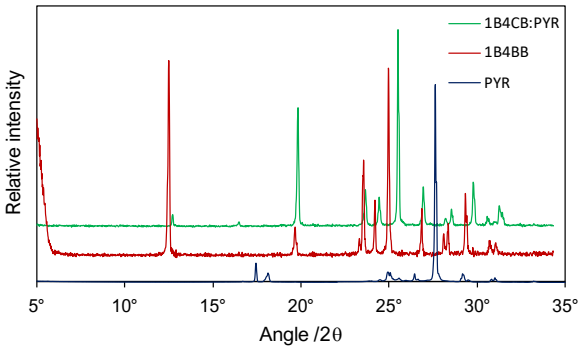

Figure S 6. 1B4CB$_2$:PYR

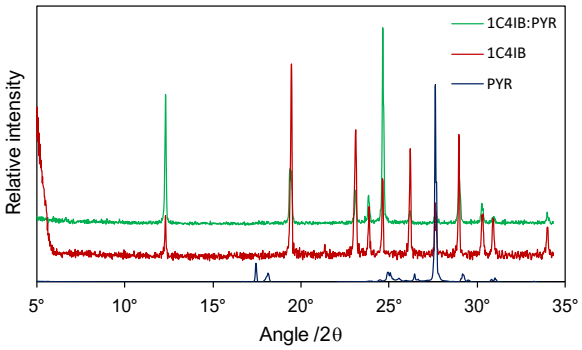

Figure S 7. 1C4IB$_2$:PYR

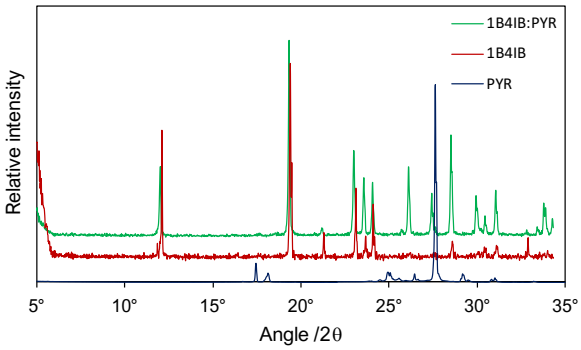

Figure S 8. 1B4IB$_2$:PYR

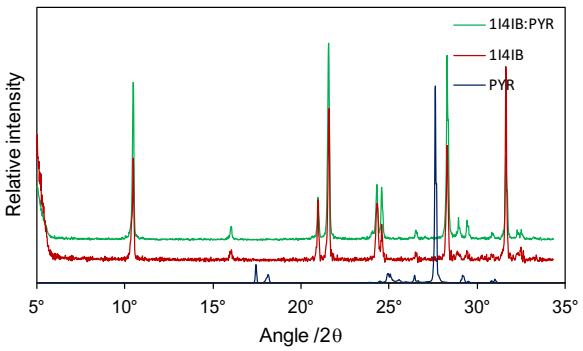

Figure S 9. 1I4IB$_2$:PYR

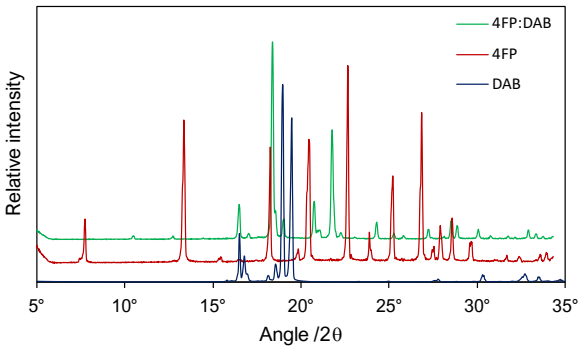

Figure S 10. 4FP$_2$:DAB

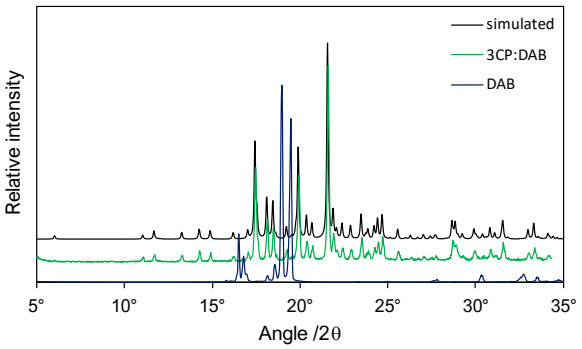

Figure S 11. 3CP$_2$:DAB

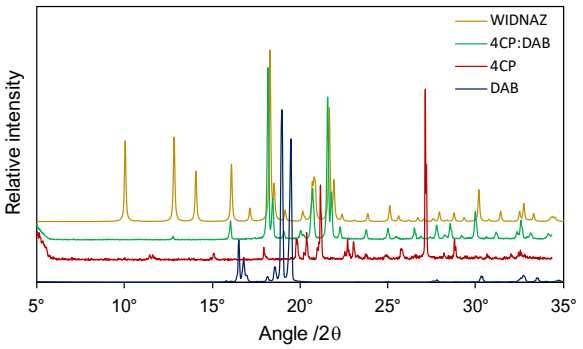

Figure S 12. 4CP$_2$:DAB

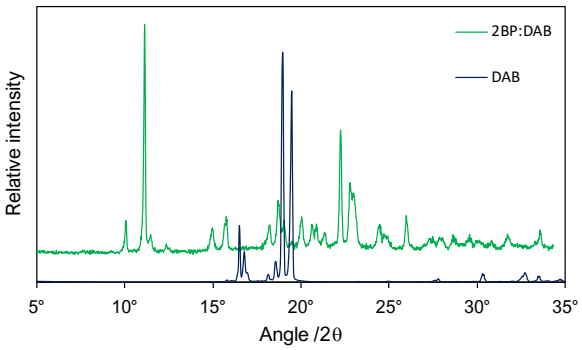

Figure S 13. 2BP$_2$:DAB

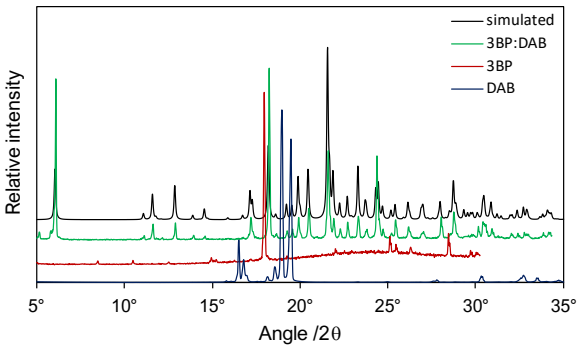

Figure S 14. 3BP$_2$:DAB

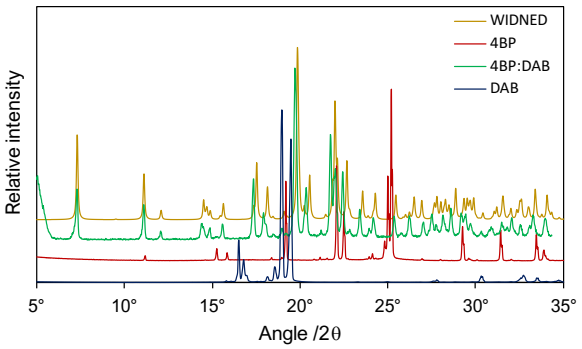

Figure S 15. 4BP$_2$:DAB

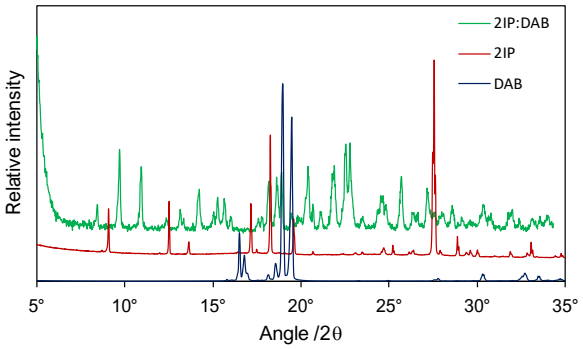

Figure S 16. $2IP_2$:DAB

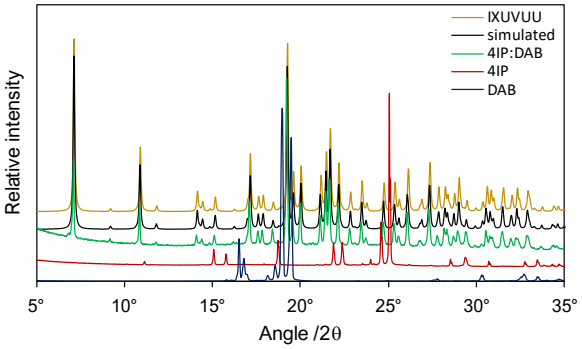

Figure S 17. $4IP_2$:DAB

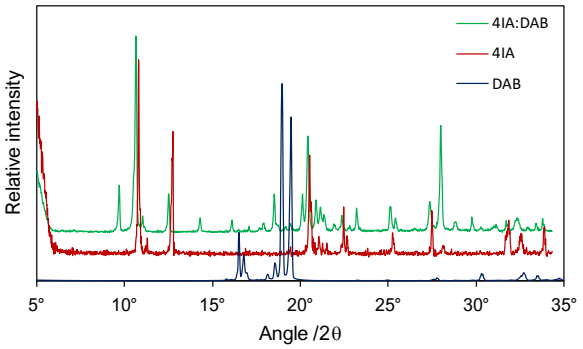

Figure S 18. $4IA_2$:DAB

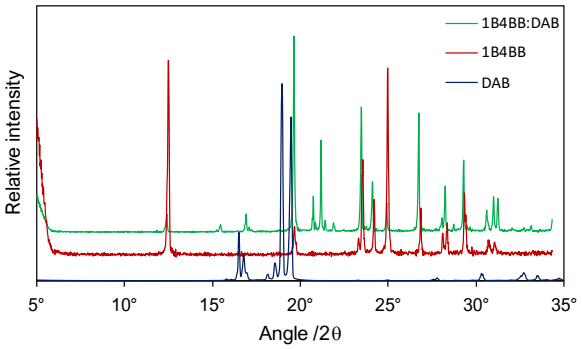

Figure S 19. $1B4BB_2$:DAB

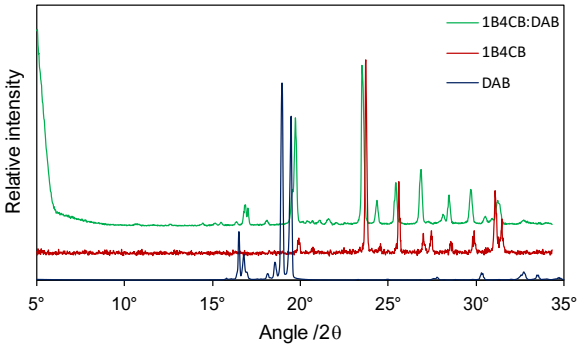

Figure S 20. $1B4CB_2$:DAB

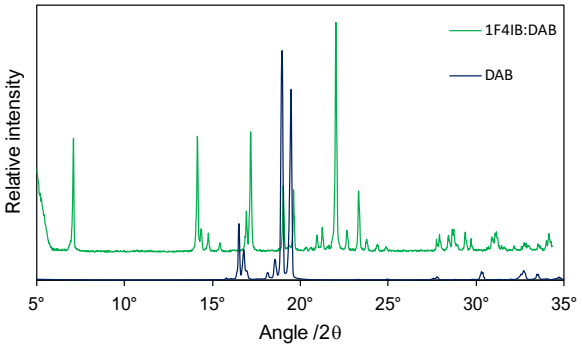

Figure S 21. $1F4IB_2$:DAB

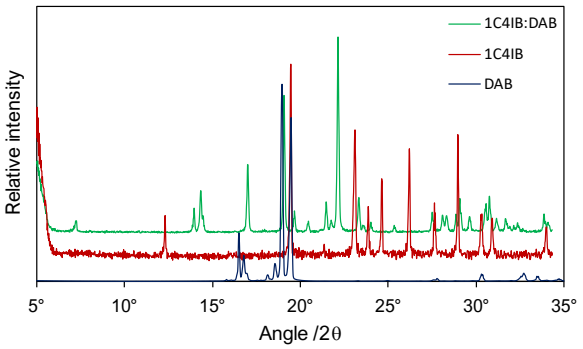

Figure S 22. $1C4IB_2$:DAB

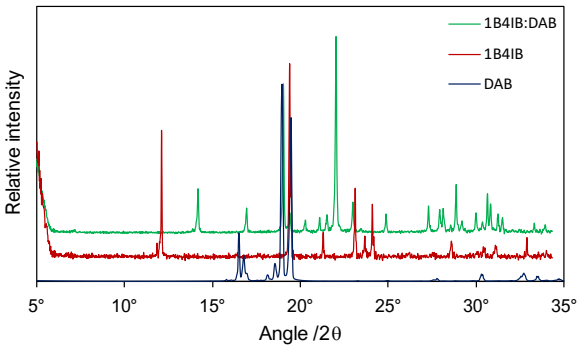

Figure S 23. $1B4IB_2$:DAB

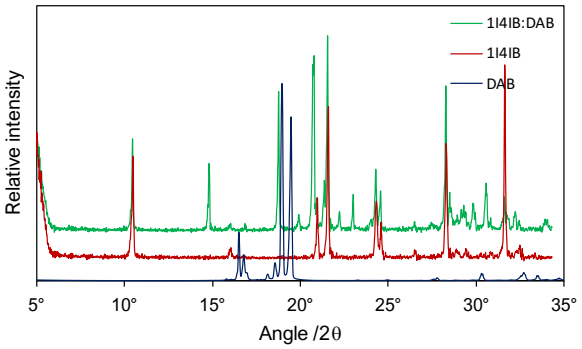

Figure S 24. 1I4IB$_2$:DAB

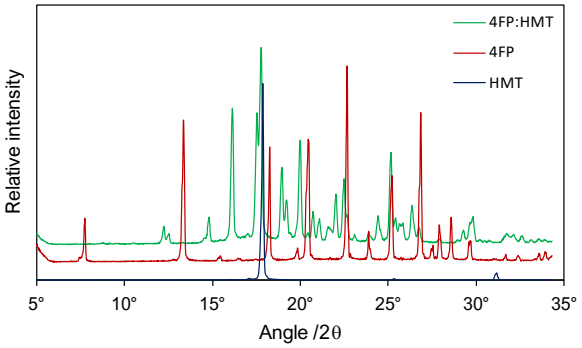

Figure S 25. 4FP$_2$:HMT

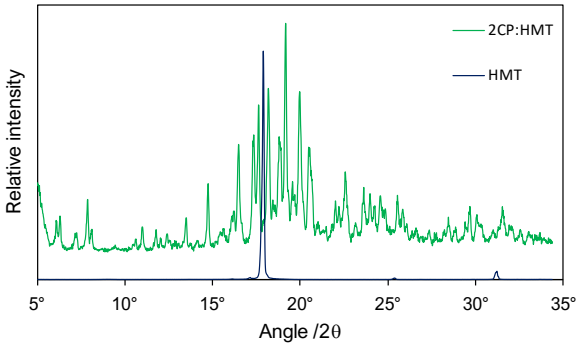

Figure S 26. 2CP$_2$:HMT

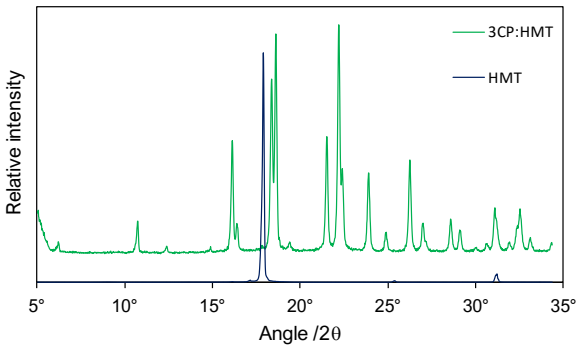

Figure S 27. 3CP$_2$:HMT

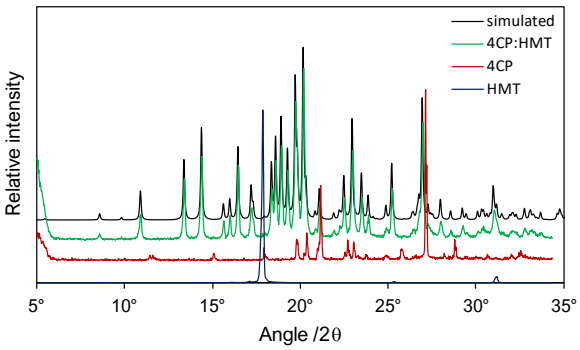

Figure S 28. 4CP$_2$:HMT

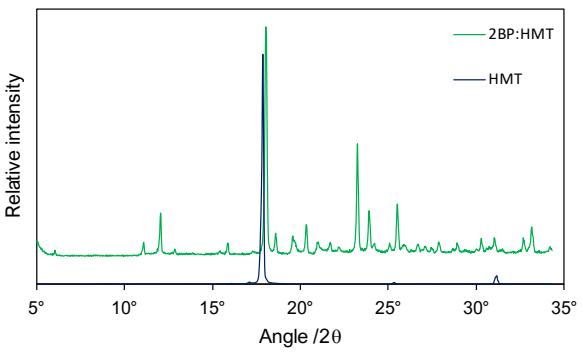

Figure S 29. 2BP$_2$:HMT

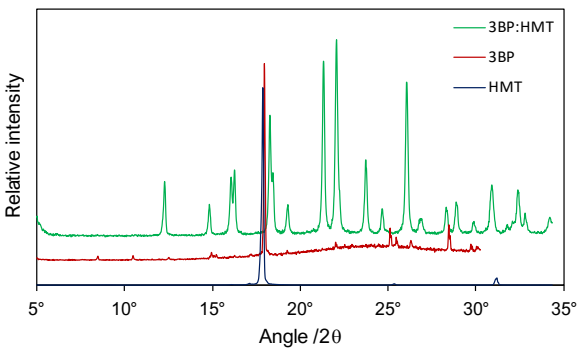

Figure S 30. 3BP$_2$:HMT

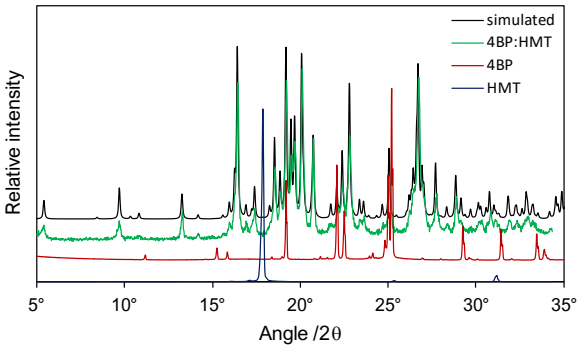

Figure S 31. 4BP$_2$:HMT

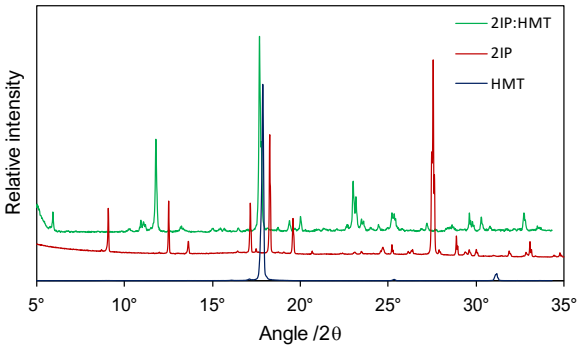

Figure S 32. 2IP$_2$:HMT

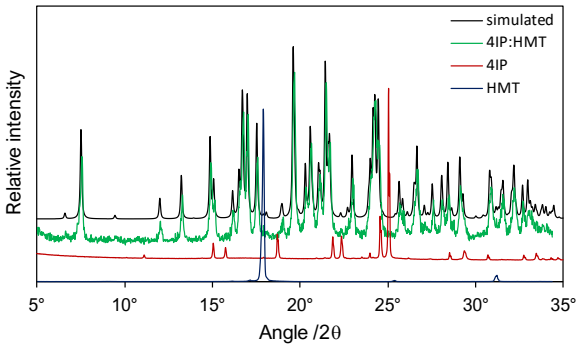

Figure S 33. 4IP$_2$:HMT

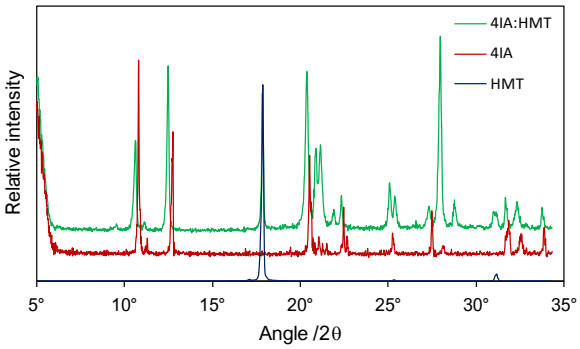

Figure S 34. 4IA$_2$:HMT

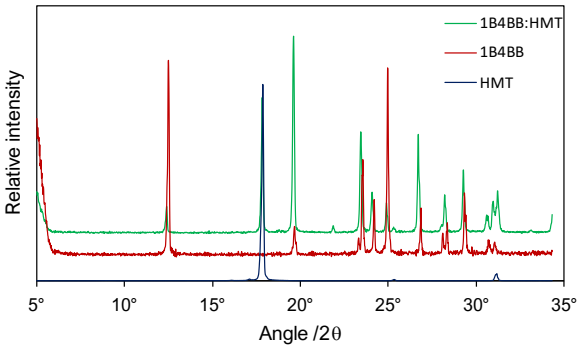

Figure S 35. 1B4BB$_2$:HMT

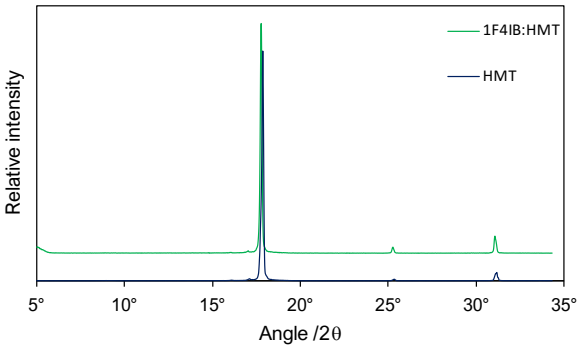

Figure S 36. 1F4IB$_2$:HMT

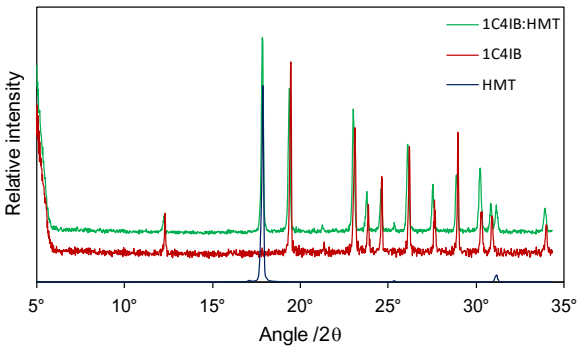

Figure S 37. 1C4IB$_2$:HMT

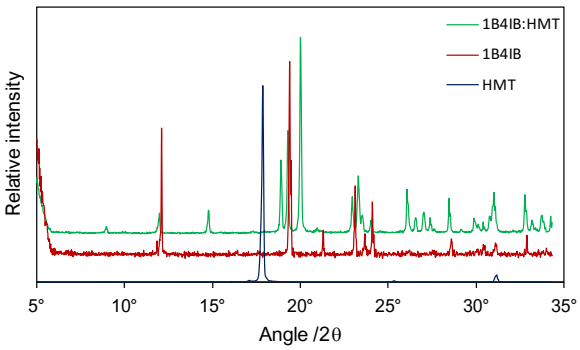

Figure S 38. 1B4IB$_2$:HMT

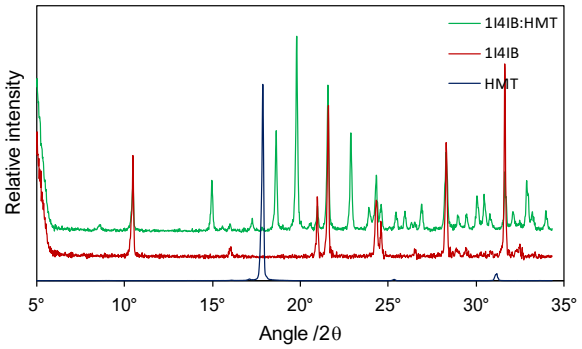

Figure S 39. 1I4IB$_2$:HMT

Tables S1-S6: Solution calorimetry results

Table S 1. Solution calorimetry results for the dissolution of THC in DMSO (reaction 2.7), ε = 7.236 ± 0.019 mJ·mV^{-1}·s^{-1}.

m_{THC} /mg	m_{DMSO} /g	n_{DMSO} /n_{THC}	A /mV·s	$\Delta_{sol}h$ /J·g^{-1}
7.8472	16.71853	8176	-11.385	25.172
6.1607	16.74061	10428	-6.077	25.828
7.7205	16.78942	8346	-8.541	22.919
7.2005	16.77886	8943	-5.600	21.619
7.0040	16.75556	9181	-5.932	22.569

Table S 2. Solution calorimetry results for the dissolution of CEL in THC:DMSO solution (reaction 2.8), ε = 7.342 ± 0.021 mJ·mV^{-1}·s^{-1}.

m_{CEL} / mg	$m_{THC:DMSO}$ /g	n_{DMSO} / n_{CEL}	A /mV·s	$\Delta_{sol}h$ /J·g^{-1}
8.9059	17.07569	9355.8	12.863	2.514
8.0356	16.80499	10204.7	12.806	2.839
8.8213	16.81767	9302.8	13.458	2.043
6.6147	16.77645	12375.7	14.546	1.517
8.9014	16.79718	9207.9	14.311	1.321

Table S 3. Solution calorimetry results for the dissolution of CTC in DMSO (reaction 2.6), ε = 7.176 ± 0.030 mJ·mV^{-1}·s^{-1}.

$m_{THC:CEL}$ /mg	m_{DMSO} /g	n_{DMSO} / $n_{THC:CEL}$	A /mV·s	$\Delta_{sol}h$ /J·g^{-1}
13.8604	16.75076	10537	-19.025	18.089
14.4042	16.73986	10133	-20.558	18.169
12.8408	16.74563	11370	-16.866	18.318
12.7762	16.71792	11409	-19.250	19.750
12.6724	16.71560	11501	-18.061	19.238

Table S 4. Solution calorimetry results for the dissolution of COA300 in DMSO (reaction 2.6), ε = 7.250 ± 0.020 mJ·mV^{-1}·s^{-1}.

m_{COA300} /mg	m_{DMSO} /g	n_{DMSO} / $n_{THC:CEL}$	A /mV·s	$\Delta_{sol}h$ /J·g^{-1}
8.9016	16.73161	16388	51.587	-28.758
9.1968	16.74295	15873	46.118	-23.568
8.4282	16.74692	17325	42.327	-22.49
8.4132	16.75077	17360	47.395	-26.852
8.461	16.72972	17240	43.121	-23.076

Table S 5. Solution calorimetry results for the dissolution of COA900 in DMSO (reaction 2.6), ε = 7.250 ± 0.020 mJ·mV^{-1}·s^{-1}.

m_{COA900} /mg	m_{DMSO} /g	n_{DMSO} / $n_{THC:CEL}$	A /mV·s	$\Delta_{sol}h$ /J·g^{-1}
8.2811	16.74969	17635	44.377	-24.666
9.6802	16.75235	15089	50.051	-25.307
10.5928	16.75056	13787	49.373	-22.667
8.8865	16.73034	16415	41.813	-20.915
8.8286	16.71602	16508	41.609	-20.886

Table S 6. Solution calorimetry results for the dissolution of CTC(SD) in DMSO (reaction 2.6), ε = 7.250 ± 0.020 mJ·mV^{-1}·s^{-1}.

$m_{CTC(SD)}$ /mg	m_{DMSO} /g	n_{DMSO} / $n_{THC:CEL}$	A /mV·s	$\Delta_{sol}h$ /J·g^{-1}
9.3138	16.78105	15709	-0.826	7.812
10.6469	16.77953	13741	-4.681	10.331
9.3895	16.78846	15590	-2.322	8.951
11.1675	16.78724	13107	-1.259	7.985
10.0408	16.80701	14595	-4.261	10.221